JOURNAL OF PETROLOGY | VOLUME 55 | NUMBER 6 | PAGES 1173–1201 | 2014 | doi:10.1093/petrology/egu022

Magmatic Processes and Associated Timescales Leading to the January 1835 Eruption of Cosigüina Volcano, Nicaragua

MARC-ANTOINE LONGPRÉ[1,2]*, JOHN STIX[2], FIDEL COSTA[3], EVELING ESPINOZA[4] AND ANGÉLICA MUÑOZ[4]

[1]SCHOOL OF EARTH AND ENVIRONMENTAL SCIENCES, QUEENS COLLEGE, CITY UNIVERSITY OF NEW YORK, 65–30 KISSENA BOULEVARD, FLUSHING, NY 11367, USA

[2]DEPARTMENT OF EARTH AND PLANETARY SCIENCES, MCGILL UNIVERSITY, 3450 UNIVERSITY STREET, MONTRÉAL, QC, H3A 0E8, CANADA

[3]EARTH OBSERVATORY OF SINGAPORE, NANYANG TECHNOLOGICAL UNIVERSITY, SINGAPORE 639798, SINGAPORE

[4]INSTITUTO NICARAGÜENSE DE ESTUDIOS TERRITORIALES (INETER), APARTADO POSTAL 2110, MANAGUA, NICARAGUA

RECEIVED FEBRUARY 28, 2013; ACCEPTED APRIL 4, 2014

Cosigüina volcano, in northwestern Nicaragua, erupted violently on 20–24 January 1835, producing pumice, scoria, ash fall deposits, and pyroclastic flows with a bulk tephra volume of ~6 km^3. New geochemical data are presented for bulk-rocks, matrix glasses, melt inclusions and minerals from the 1835 deposits and a pre-1835 basaltic andesite tephra, with the aim of shedding light on the magmatic processes and associated timescales that led to the eruption. Our results reveal that the 1835 eruption was fed by a compositionally and thermally zoned magma reservoir situated ~4 km (P_{H2O} ~100 MPa) beneath the volcano. Small volumes of crystal-poor dacite (<10 wt % phenocrysts, 63·8–64·8 wt % SiO_2, ~950°C) and silicic andesite (<10 wt % phenocrysts, 62·2 wt % SiO_2, 960–1010°C) were erupted first, followed by relatively crystal-rich andesite (15–30 wt % phenocrysts, 57·4–58·8 wt % SiO_2, 960–1010°C), which accounts for ~90% of the erupted magma. The pre-1835 basaltic andesite (~20 wt % phenocrysts, 52·4 wt % SiO_2, 1110–1170°C) represents a mafic end-member for Cosigüina. The major and trace element compositions of the bulk-rocks, melt inclusions and matrix glasses suggest that (1) the pre-1835 basaltic andesite is a plausible parent for the 1835 magmas, (2) the 1835 andesite bulk-rocks do not represent true melts, but instead mixtures of silicic andesite liquid and a component of accumulated crystals dominated by plagioclase, and (3) the silicic andesite and dacite formed from the andesite magma through liquid extraction followed by fractional crystallization. Observed bimodal to trimodal crystal populations are consistent with a multi-stage, polybaric differentiation process, with calcic plagioclase ($An_{75–90}$, $An_{90–95}$) and magnesian clinopyroxene (Mg# = 67–75), plus olivine and magnetite, forming from mafic andesite, basaltic andesite and basalt in the lower crust. The calcic plagioclase exhibits sieve textures, which may be the result of H_2O-undersaturated decompression during magma ascent to the upper crust; $An_{50–65}$ plagioclase lacking a sieve texture, orthopyroxene (Mg# = 61 and 63–72), clinopyroxene (Mg# = 67), magnetite and apatite crystallized from andesite to dacite liquids in the shallow magma reservoir. $An_{75–90}$ plagioclase comprising entire phenocrysts or cores with $An_{50–65}$ rims in the 1835 magmas is cognate from earlier stages of differentiation and shows evidence of extensive diffusion of Mg when compared with similar $An_{75–95}$ crystals hosted in the pre-1835 basaltic andesite. Using plagioclase–melt Mg partitioning and modelling of the Mg diffusion process, we constrain the residence time of these crystals in the silicic liquids to more than 100 years and less than 2000 years, with detailed analysis of three crystals yielding ~400 years. We propose that magma reservoir zonation occurred on timescales of 10^2–10^3 years at Cosigüina. The occurrence of H_2O-rich fluid inclusions in all 1835 samples and volatile element systematics in melt inclusions imply that the magmas were saturated with a vapour phase (H_2O, S, ± CO_2) during much of their evolution in the upper

*Corresponding author. Telephone: +1 718 997 3259. E-mail: mlongpre@qc.cuny.edu

crust. Accumulation of free gas at the top of the magma reservoir may have led to overpressurization of the system, triggering the eruption. Catastrophic release of this exsolved vapour and syn-eruptive devolatilization of the melt injected several teragrams of S into the atmosphere. Our data, coupled with independent evidence from ice cores and tree rings, indicate that the Cosigüina eruption had a sizeable atmospheric impact comparable with or larger than that of the 1991 Pinatubo eruption. Stratigraphic evidence shows that Cosigüina has produced >15 compositionally zoned explosive eruptions in the past, suggesting that similar future eruptions are likely. The products of the 1835 eruption of Cosigüina share many features with compositionally zoned eruptive sequences elsewhere, such as the climactic eruption of Mount Mazama, the AD 79 'Pompei' eruption of Vesuvius and the 1912 eruption of Novarupta–Katmai.

KEY WORDS: *andesite; compositionally zoned magma reservoir; Cosigüina volcano; plagioclase; timescales of magmatic processes*

INTRODUCTION

Explosive volcanic eruptions are fuelled by gas-rich magmas stored in reservoirs and transported through conduits. Understanding the subsurface magma plumbing systems feeding explosive volcanoes ultimately contributes to eruption forecasting and is thus a central goal of volcanology (e.g. Sparks, 2003). Although geophysical monitoring of currently active volcanoes yields crucial insights into the workings of magma plumbing systems, volcanologists must turn to other methods to study dormant, but potentially hazardous volcanoes. Studies of historical and prehistoric eruptive products can provide a wealth of information on the physico-chemical conditions that led to past eruptions. Determination of the temperature and pressure of magma storage, the pre-eruptive volatile element contents of magmas, and the processes and associated timescales that cause chemical differentiation of magmas yield very useful data when evaluating potential eruptive scenarios at long-dormant, explosive volcanoes (e.g. Blundy & Cashman, 2008).

Cosigüina volcano forms a peninsula at the northwestern tip of Nicaragua and consists of a voluminous composite cone culminating at 872 m above sea level. It features a 2·5 km wide, >500 m deep summit caldera that contains a large emerald lake (Fig. 1). The volcano's other characteristics of note include, with all distances relative to the caldera rim: (1) ~4 km ESE, a broad ridge of lava flows (Loma San Juan) that appears to predate Cosigüina; (2) ~2 km west, a prominent arcuate ridge interpreted as the vestige of a truncated proto-Cosigüina edifice; (3) ~5 km SW, a NW–SE linear structure that may represent the trace of a fault; (4) ~3 km north, an ~1 km wide maar volcano (see also Williams, 1952; Scott *et al.*, 2006; Hradecký & Rapprich, 2008). Cosigüina is best known for its brief but extremely violent eruption in January 1835 that sent ash to Mexico, Costa Rica, and perhaps as far as Colombia and Jamaica, and produced explosions heard as far as Belize and Colombia (Galindo, 1835*a*, 1835*b*; Caldcleugh, 1836). Initial estimates of tephra volume reached 50–150 km^3 (e.g. Reclus, 1891), but were later shown to have been greatly exaggerated (Williams, 1952; Self *et al.*, 1989). Stratigraphic surveys by Scott *et al.* (2006) on the flanks of the volcano indicated a bulk tephra volume of ~6 km^3 [Volcanic Explosivity Index (VEI) = 5, Newhall & Self, 1982], ranking the 1835 event among the Americas' largest and most explosive historical eruptions, after those of Huaynaputina, Peru, in 1600, Santa Maria, Guatemala, in 1902, Novarupta–Katmai, Alaska, in 1912 and Quizapu, Chile, in 1932 (Siebert & Simkin, 2002). Other than the 1835 event, Siebert & Simkin (2002) listed eruptions at Cosigüina in 1609 (uncertain), 1709 and 1809 (uncertain, possible confusion with the 1709 eruption), as well as in 1852 and 1859, which were probably small. The volcano has been dormant since the 19th century, although a swarm of seismic events, probably of volcano-tectonic origin, occurred nearby in September 2002 (Siebert & Simkin, 2002).

The sequence of events proposed by Self *et al.* (1989) and Scott *et al.* (2006), based on correlations between eyewitness accounts and stratigraphy, indicates that the first phase of the 1835 eruption began on the morning of 20 January, producing a thin dacite pumice to silicic andesite scoria fall dispersed to the north and NW and basal ash elsewhere around the volcano. After an apparent lull during the night of 20–21 January, the second and main phase of the eruption began in the morning of 21 January, lasting all day. This vigorous activity produced the prominent andesite scoria fall that is present on all flanks of the volcano and is thickest to the north and NE. The third phase, from 22 to 24 January and possibly to the end of the month, involved further explosive activity producing widespread ash fall and pyroclastic flows, the latter affecting the northern, eastern and southern flanks of Cosigüina. On the basis of centimetre-sized scoria fall 35 km north of Cosigüina during phase 2, Self *et al.* (1989) estimated peak eruption column heights in excess of 25 km. The thicknesses of pumice and scoria fall deposits reported by Scott *et al.* (2006) imply that the dacite and silicic andesite represent ~10% of the magma erupted, and the andesite ~90%.

Misguided by the early eruptive volume estimates, a number of workers assumed that the Cosigüina eruption had global atmospheric effects that were responsible for cool surface temperature in the mid- to late 1830s (Lamb, 1970; Angell & Korshover, 1985). Based on the revised eruptive volume, apparently low sulphur yield (Palais & Sigurdsson, 1989) and ambiguous climate trends of the 1830s, Self *et al.* (1989) argued that the climatic impact of the Cosigüina eruption had in fact been small to

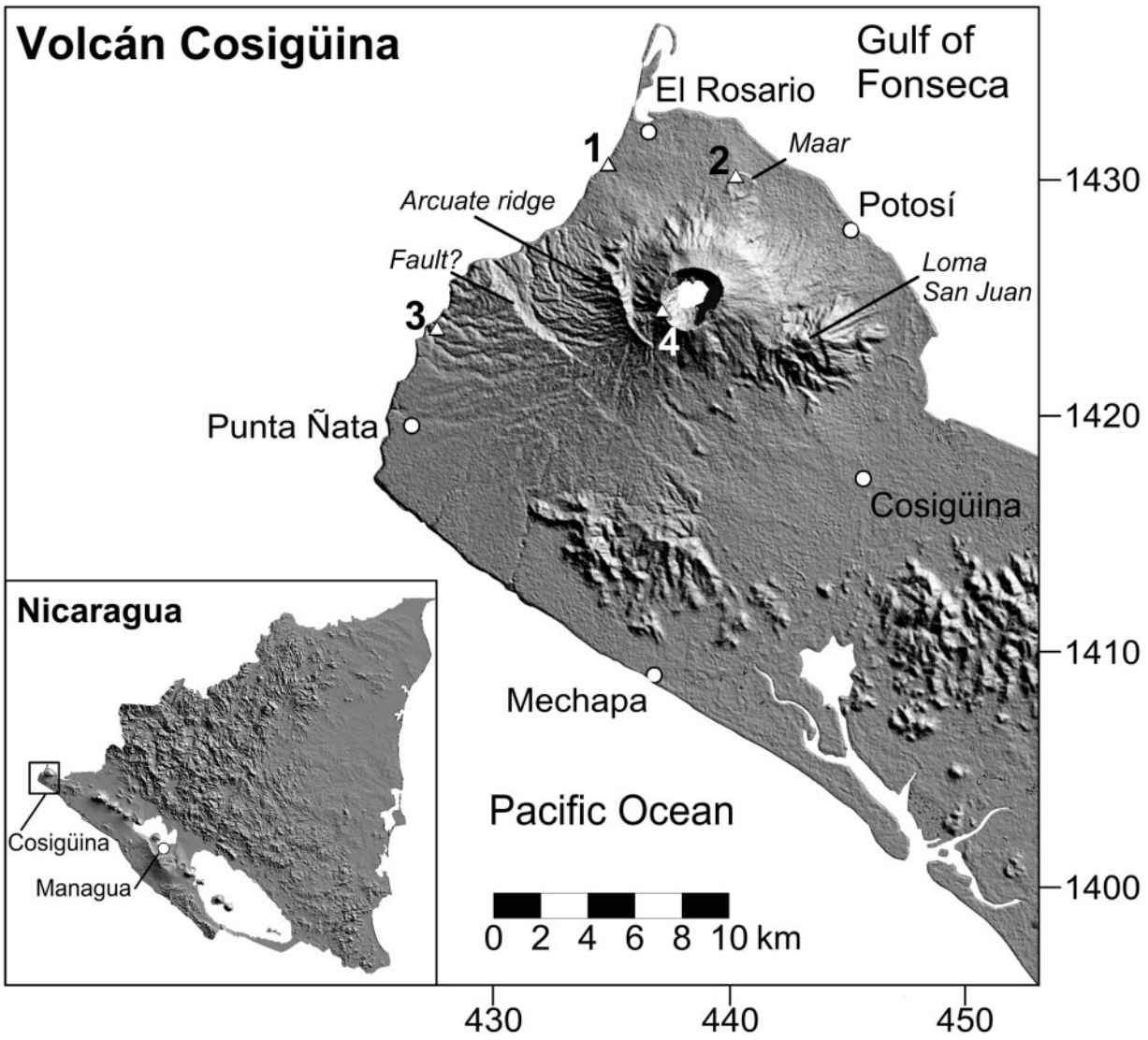

Fig. 1. Digital elevation model of Cosigüina volcano. UTM coordinates in km, WGS84 datum. Sampling localities for this study (triangles) and main villages (circles) of the Cosigüina peninsula are shown. The inset indicates the position of Cosigüina at the NW tip of Nicaragua's volcanic front.

negligible. Nevertheless, subsequent studies of ice cores from both the Arctic and Antarctic (e.g. Gao *et al.*, 2008) and temperature-sensitive tree-ring chronologies (e.g. Briffa *et al.*, 1998) provide new evidence of substantial stratospheric sulphur injection and associated surface cooling owing to the eruption.

This study presents new geochemical data on bulk-rocks, matrix glasses, melt inclusions and minerals from the 1835 deposits, with the aim of shedding light on the conditions and magma reservoir processes and associated timescales that led to the eruption. In a companion paper (Longpré *et al.*, in preparation), we re-evaluate the eruption's sulphur discharge to the atmosphere and its effect on the global climate of the mid- to late 1830s.

SAMPLING AND ANALYTICAL METHODS

Sampling

We sampled the 1835 eruptive products at four main localities previously described by Scott *et al.* (2006) (Fig. 1). Compositional zoning of the pyroclastic fall deposits is best exposed at locality 1, where representative samples were collected from all stratigraphic units (Fig. 2). At locality 2, where the 1835 deposits are well exposed against the inner crater wall of a maar volcano, we collected additional samples of the dacite pumice and andesite scoria. Locality 3 exposes numerous prehistoric tephras beneath the 1835 ash and scoria fall; this remarkably complete stratigraphic section will be the subject of a subsequent

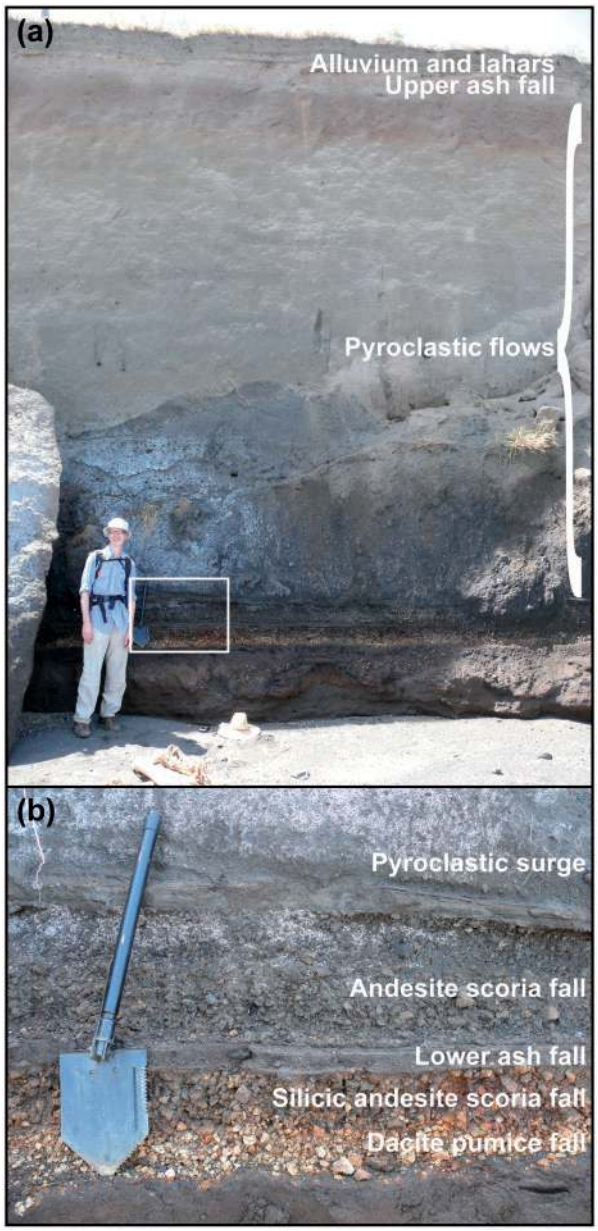

Fig. 2. Field photographs of the 1835 deposits at locality 1 (Fig. 1). (a) Complete coastal section of the 1835 deposits, from the dacite pumice to the post-eruptive alluvium and lahars. This closely corresponds to locality L described by Scott *et al.* (2006). The thick pyroclastic flow deposits should be noted. The white rectangle corresponds to the area shown in (b). (b) Close-up of the pumice and scoria fall deposits sampled for this study. The lower ash fall that separates the silicic andesite scoria from the andesite scoria should be noted.

study. Here we use a mafic scoria (COS-H-36) sampled near the top of this section to represent the mafic end-member of the pre-1835 activity. A sample of crater wall agglutinate associated with the 1835 eruption was also taken at locality 4.

Because the outcrop at locality 1 is partly inundated by seawater during high tides, these samples were soaked in distilled water for several weeks prior to analysis to dissolve any salt crystals that may have accumulated in vesicles. Comparison of data for samples from locality 1 and locality 2 confirms the chemically pristine state of the locality 1 samples (e.g. COS-A-1 vs COS-M-63, unaffected by seawater; Table 1).

XRF and ICP-MS

Bulk-rock major and trace element data were acquired by X-ray fluorescence (XRF) on a Philips PW2440 4 kW spectrometer at McGill University. Bulk-rock rare earth element (REE) concentrations were determined by inductively coupled plasma mass spectrometry (ICP-MS) using a PerkinElmer/SCIEX Elan 6100 DRCplus instrument at McGill University. Two internal standards, UTR-2 and SR-7, were used for both XRF and ICP-MS analyses (Supplementary Data Table A1; supplementary material is available for downloading at http://www.petrology.oxfordjournals.org).

Electron microprobe

Major element and volatile element concentrations for minerals, matrix glasses and melt inclusions were obtained using a JEOL 8900 electron microprobe at McGill University. Analytical conditions varied depending on the material of interest. Overall, replicate analyses of well-characterized mineral and glass standards during each analytical session indicate that the measurements are accurate to better than 5% for major elements (concentration >1 wt %) and to better than 10% for minor elements (concentration <1 wt %).

Glasses and the volatiles-by-difference method

The conditions used for the analysis of Cosigüina glasses were chosen to maximize the precision and accuracy of the volatiles-by-difference method. Devine *et al.* (1995) discussed the advantages and limitations of this technique for estimating H_2O contents of silicic glasses. Despite limited accuracy and precision (>0·5 wt %), the method is useful for water-rich samples. This was corroborated by Humphreys *et al.* (2006), who obtained excellent correlation between ion microprobe and volatiles-by-difference results for hydrous silicic glasses, with acceptable accuracy (0·6 wt %) and precision (0·8 wt %). Those workers emphasized the importance of using low beam current and large beam diameter to minimize damage to the glasses. We used these recommended analytical conditions (15 kV accelerating voltage, 2 nA current and 15 μm beam diameter) and performed tests to confirm that Na migration did not occur in the most silicic glass inclusions. Data were acquired over 2–3 spots within single inclusions, for total counting times of 20–30 s for Na (analysed first), 160–240 s for S, 120–180 s for Cl and 40–60 s for all other elements. To assess the accuracy and precision of our method for water in particular, we used a set of

Table 1: Major (in wt %) and trace (in ppm) element compositions of bulk-rocks, matrix glasses and melt inclusions obtained by XRF and EMP

Sample:	COS-A-1	COS-M-63	COS-A-1	COS-A-1	COS-A-2	COS-A-2	COS-A-2	COS-A-3	COS-A-5a
Deposit:	Pumice fall	Pumice fall	Pumice fall	Pumice fall	Scoria fall	Scoria fall	Scoria fall	Lithic	Scoria fall
Analysis:	Dacite bulk	Dacite bulk	Dacite glass	Dacite MI	Silicic andesite bulk	Silicic andesite glass	Silicic andesite MI	Bulk	Andesite bulk
			$n=30$	$n=9$		$n=25$	$n=14$		
Locality:[1]	1	2	1	1	1	1	1	1	1
SiO_2	62·60	63·02	65·58 (0·37)	63·18 (1·92)	61·10	62·17 (1·53)	58·54 (2·11)	53·10	58·04
TiO_2	0·70	0·71	0·62 (0·09)	0·78 (0·17)	0·80	0·82 (0·17)	0·93 (0·20)	0·90	0·75
Al_2O_3	15·20	15·54	15·51 (0·20)	15·15 (0·62)	15·71	15·57 (0·45)	15·07 (0·91)	19·36	17·88
FeO*	5·96	6·24	5·88 (0·19)	5·92 (1·38)	6·96	7·60 (1·03)	7·71 (1·37)	8·76	6·96
MnO	0·20	0·17	0·15 (0·04)	0·18 (0·12)	0·19	0·19 (0·04)	0·19 (0·06)	0·17	0·17
MgO	1·30	1·41	1·11 (0·06)	1·04 (0·42)	1·87	1·82 (0·39)	2·12 (0·59)	2·98	2·12
CaO	4·10	4·42	3·90 (0·11)	3·80 (0·77)	5·03	4·97 (0·58)	4·77 (0·53)	9·75	7·01
Na_2O	4·20	4·25	4·83 (0·20)	4·22 (0·25)	4·56	4·38 (0·30)	3·79 (0·68)	2·89	4·14
K_2O	2·10	2·00	2·20 (0·07)	2·06 (0·29)	1·78	1·97 (0·27)	1·84 (0·54)	1·01	1·47
P_2O_5	0·30	0·27	0·22 (0·02)	0·23 (0·04)	0·28	0·29 (0·04)	0·23 (0·06)	0·17	0·22
Total	96·66	98·02	100·02	96·57	98·28	99·77	95·17	99·09	98·76
LOI	2·48	1·04			0·93			0·39	0·68
S			150 (60)	260 (100)		190 (180)	480 (140)		
Cl			2380 (210)	2540 (210)		1860 (230)	2120 (440)		
H_2O[2]			−0·3 (1·0)	3·4 (1·9)		0·0 (0·7)	4·6 (2·3)		
Ba	1200	1176			1079			671	882
Ce	b.d.l.	17			30			28	31
Co	14	18			18			30	19
Cr	18	23			17			16	15
Cu	65	92			45			190	64
Ni	b.d.l.	b.d.l.			3			5	3
Sc	14	13			14			26	19
V	47	50			91			276	131
Zn	56	55			60			52	39
Ga	15	16			16			19	16
Nb	2	3			2			1	2
Pb	6	6			5			3	4
Rb	40	39			34			18	27
Sr	301	312			339			415	397
Th	2	2			1			1	2
U	3	b.d.l.			3			1	2
Y	37	37			34			23	28
Zr	149	146			129			70	103

(continued)

Table 1: Continued

Sample:	COS-A-5b	COS-A-5b	COS-A-5b	COS-A-8	COS-C-11	COS-M-50	COS-N-75	COS-H-36	COS-H-36	COS-H-36
Deposit:	Scoria fall	Scoria fall	Scoria fall	Pyroclastic flow	Pyroclastic flow	Scoria fall	Agglutinate	Scoria fall	Scoria fall	Scoria fall
Analysis:	Andesite bulk	Andesite glass $n=21$	Andesite MI $n=25$	Andesite bulk	Andesite bulk	Andesite bulk	Andesite bulk	Basaltic bulk	Basaltic andesite glass $n=25$	Basaltic andesite MI $n=12$
Locality:[1]	1	1	1	1	1	2	4	3	3	3
SiO_2	56·87	61·92 (0·93)	58·57 (1·38)	57·16	58·38	57·95	57·64	52·02	53·66 (0·36)	52·99 (1·04)
TiO_2	0·75	0·82 (0·18)	0·88 (0·17)	0·74	0·76	0·75	0·74	0·88	1·11 (0·10)	1·13 (0·22)
Al_2O_3	18·82	15·64 (0·51)	15·14 (0·67)	18·57	18·12	18·42	18·39	18·39	15·56 (0·18)	15·01 (0·35)
FeO*	7·05	7·62 (0·52)	8·10 (0·80)	6·96	7·03	7·01	7·01	9·92	11·88 (0·28)	11·37 (0·36)
MnO	0·17	0·19 (0·04)	0·19 (0·05)	0·17	0·18	0·17	0·17	0·20	0·23 (0·04)	0·21 (0·04)
MgO	2·25	1·97 (0·24)	2·54 (0·38)	2·23	2·14	2·13	2·13	4·48	4·55 (0·12)	4·32 (0·56)
CaO	7·89	5·20 (0·38)	5·19 (0·54)	7·70	7·22	7·44	7·46	9·90	8·52 (0·13)	7·92 (0·49)
Na_2O	3·77	4·23 (0·25)	3·84 (0·40)	4·05	3·88	3·77	3·72	2·52	3·18 (0·27)	2·93 (0·16)
K_2O	1·26	1·99 (0·23)	1·72 (0·29)	1·26	1·41	1·35	1·36	0·73	1·00 (0·06)	1·08 (0·13)
P_2O_5	0·21	0·27 (0·03)	0·25 (0·04)	0·21	0·22	0·22	0·22	0·16	0·19 (0·02)	0·19 (0·03)
Total	99·04	99·84	96·39	99·05	99·34	99·21	98·84	99·20	99·87	97·15
LOI	0·63			0·70	0·00	0·00	0·25	0·00		
S		130 (40)	580 (120)						60 (70)	480 (300)
Cl		1650 (350)	1790 (330)						960 (110)	1240 (290)
H_2O[2]		0·0 (0·8)	3·3 (1·7)						0·0 (0·8)	2·6 (1·0)
Ba	803			822	890	851	814	528		
Ce	28			26	26	35	22	20		
Co	20			20	21	15	20	28		
Cr	16			b.d.l.	14	11	21	18		
Cu	78			66	60	141	172	314		
Ni	3			b.d.l.	b.d.l.	b.d.l.	b.d.l.	8		
Sc	17			19	16	17	16	30		
V	151			141	136	139	126	315		
Zn	46			42	49	56	52	61		
Ga	17			17	17	17	17	17		
Nb	2			2	2	2	2	1		
Pb	3			2	5	5	4	2		
Rb	23			25	27	26	25	14		
Sr	422			417	403	413	406	437		
Th	1			b.d.l.	1	1	2	b.d.l.		
U	1			b.d.l.	2	2	b.d.l.	b.d.l.		
Y	26			27	28	28	28	19		
Zr	90			93	102	98	98	54		

*Fe reported as FeO.
[1]UTM coordinates (WGS84 datum) are: [434890, 1440810] for 1; [440300, 1440320] for 2; [427660, 1433850] for 3; [437190, 1434610] for 4.
[2]Dissolved H_2O estimated by the difference method.
Numbers in parentheses are 1 standard deviation of the mean of *n* analyses. MI, melt inclusions. b.d.l., below detection limit.

hydrous silicic glass standards that had been previously analysed for water by ion microprobe (PCD: $0{\cdot}17 \pm 0{\cdot}08$ wt % H_2O; M3N: $3{\cdot}95 \pm 0{\cdot}13$ wt % H_2O; M6N: $6{\cdot}38 \pm 0{\cdot}19$ wt % H_2O; Devine *et al.*, 1995). Repeated analyses ($n=13$ for each standard) during our electron microprobe sessions gave $0{\cdot}3 \pm 0{\cdot}8$ wt % (1σ)

H_2O for PCD, $3{\cdot}6 \pm 0{\cdot}6$ wt % H_2O for M3N and $7{\cdot}3 \pm 0{\cdot}5$ wt % H_2O for M6N (Supplementary Data Fig. A1). This indicates reasonable accuracy (within 0·9 wt %, and better for intermediate water contents) and precision (better than $\pm 0{\cdot}8$ wt %). In addition, we used the glass standards VG-2 (1400 ppm S, 300 ppm Cl, GeoReM database averages; Jarosewich *et al.*, 1980; Jochum *et al.*, 2005) and KN9 (3100 ppm Cl; Stix *et al.*, 1995) to monitor the quality of our results for sulphur and chlorine. We obtained average values of 1440 ± 60 ppm S and 320 ± 130 ppm Cl for VG-2 ($n = 21$) and 3000 ± 220 ppm Cl for KN9 ($n = 18$), in close agreement with accepted values (Supplementary Data Table A2).

Minerals

Plagioclase, clinopyroxene and orthopyroxene were analysed using a 15 kV accelerating voltage, 20 nA beam current, 5 μm beam diameter and 20 s counting times for all elements. Magnetite and sulphide analyses were carried out with a 20 kV accelerating voltage and 30 nA beam current. Apatite was analysed using a 15 kV accelerating voltage, 30 nA beam current and 10–15 μm beam diameter. Because of the known variation in F and Cl Kα X-ray intensity as a function of electron beam exposure time (Stormer *et al.*, 1993), F was analysed first and data for each apatite grain were collected for 20 s over three spots, for a total of 60 s counting time. For detailed traverses across selected plagioclase phenocrysts, we used a 15 kV accelerating voltage, 30 nA beam current, 2 μm beam diameter (3 μm between points) and 20 s counting times for all elements except Mg, which was measured for 60 s.

RESULTS

We first describe the textural, mineralogical and compositional characteristics of the dacite pumice, silicic andesite scoria and andesite scoria collected from the 1835 pyroclastic fall deposits, as well as the pre-1835 basaltic andesite sample. Based on these data, we then estimate the magmatic conditions that prevailed prior to eruption and the properties of the erupted magma. Finally, we use detailed analyses of plagioclase phenocrysts to demonstrate the partial equilibration of their magnesium content through diffusion and to calculate the duration of the diffusion process.

Dacite

The dacite pumice is largely composed of highly vesicular, microlite-poor glass (Fig. 3a), with scarce phenocrysts of plagioclase, clinopyroxene, orthopyroxene, magnetite and apatite that commonly occur as glomerocrysts (Fig. 3b). Melt inclusions occur in plagioclase and pyroxene and typically contain multiple bubbles. Phenocryst-hosted, H_2O-rich, fluid inclusions, typically smaller than 20 μm, and iron sulphide globules, 5–15 μm across, are also present (Fig. 3c).

A modest increase in silica content is observed from the bulk-rock (range 63·8–64·9 wt % SiO_2) to the matrix glass (64·7–66·1 wt % SiO_2), whereas melt inclusions span a wider compositional range (62·0–67·3 wt % SiO_2) (Figs 4a and 5, Table 1; major element compositions reported in the text and figures are normalized to 100% anhydrous, but are presented in their original form in the tables). Al_2O_3 and FeO* contents are similar in the bulk-rocks, matrix glass and melt inclusions (Fig. 5c and e). Among the samples studied, the dacite bulk-rocks have the lowest concentrations in compatible trace elements such as Sr, which enters plagioclase, and V, which enters magnetite, the highest concentrations in incompatible elements such as K, Rb, Zr, Ba and the REE, and the most pronounced negative Eu anomaly (Fig. 6, Tables 1 and 2). Estimates of H_2O contents by the difference method scatter about zero (average $-0{\cdot}3 \pm 1{\cdot}0$ wt %) for the matrix glass and average $3{\cdot}4 \pm 1{\cdot}9$ wt % for melt inclusions (Fig. 4b). Matrix glass and melt inclusions have similarly low sulphur (150 ± 60 and 260 ± 100 ppm, respectively) and high chlorine (2380 ± 210 and 2540 ± 450 ppm, respectively) concentrations (Fig. 4c and d).

Plagioclase phenocrysts in the dacite show two populations based on their anorthite contents [$\%An = 100 \times$ molar $Ca/(Ca + Na + K)$] and zoning patterns: (1) ~85% are $An_{50–65}$ phenocrysts that display weak oscillatory zoning, commonly forming glomerocrysts with other minerals; (2) ~15% are single phenocrysts that show abrupt normal zoning, with a thick $An_{50–65}$ rim mantling an $An_{75–90}$ core (Fig. 7a, Table 3). Rare microlites are $An_{42–46}$ plagioclase. Clinopyroxene with a mean magnesium number [$Mg\# = 100 \times$ molar $Mg/(Mg + Fe_{total})$] of 67 (Cpx_{67}), orthopyroxene ($Mg\#$ 61) and magnetite are present as single crystal populations (Fig. 8, Table 3). Apatite grains contain $1{\cdot}7 \pm 0{\cdot}1$ wt % F and 8800 ± 210 ppm Cl and are S-poor (below detection limit of ~90 ppm). Crystal contents were estimated by reproducing the glass chemistry from the bulk-rock composition through subtraction of the observed mineral phases using least-squares mass-balance calculations performed with PetroGraph (Stormer & Nicholls, 1978; Petrelli *et al.*, 2005) (Table 4). This approach indicates that the dacite pumice contains 4·6 wt % plagioclase, 0·5 wt % clinopyroxene, 1·4 wt % orthopyroxene, 0·6 wt % magnetite and 0·1 wt % apatite, for a total crystallinity of 7 wt % (vol.% values are also reported in Table 4) consistent with thin-section observations.

Silicic andesite

The silicic andesite scoria comprises moderately vesicular, microlite-rich glass and is phenocryst poor, with a mineral assemblage similar to that of the dacite pumice,

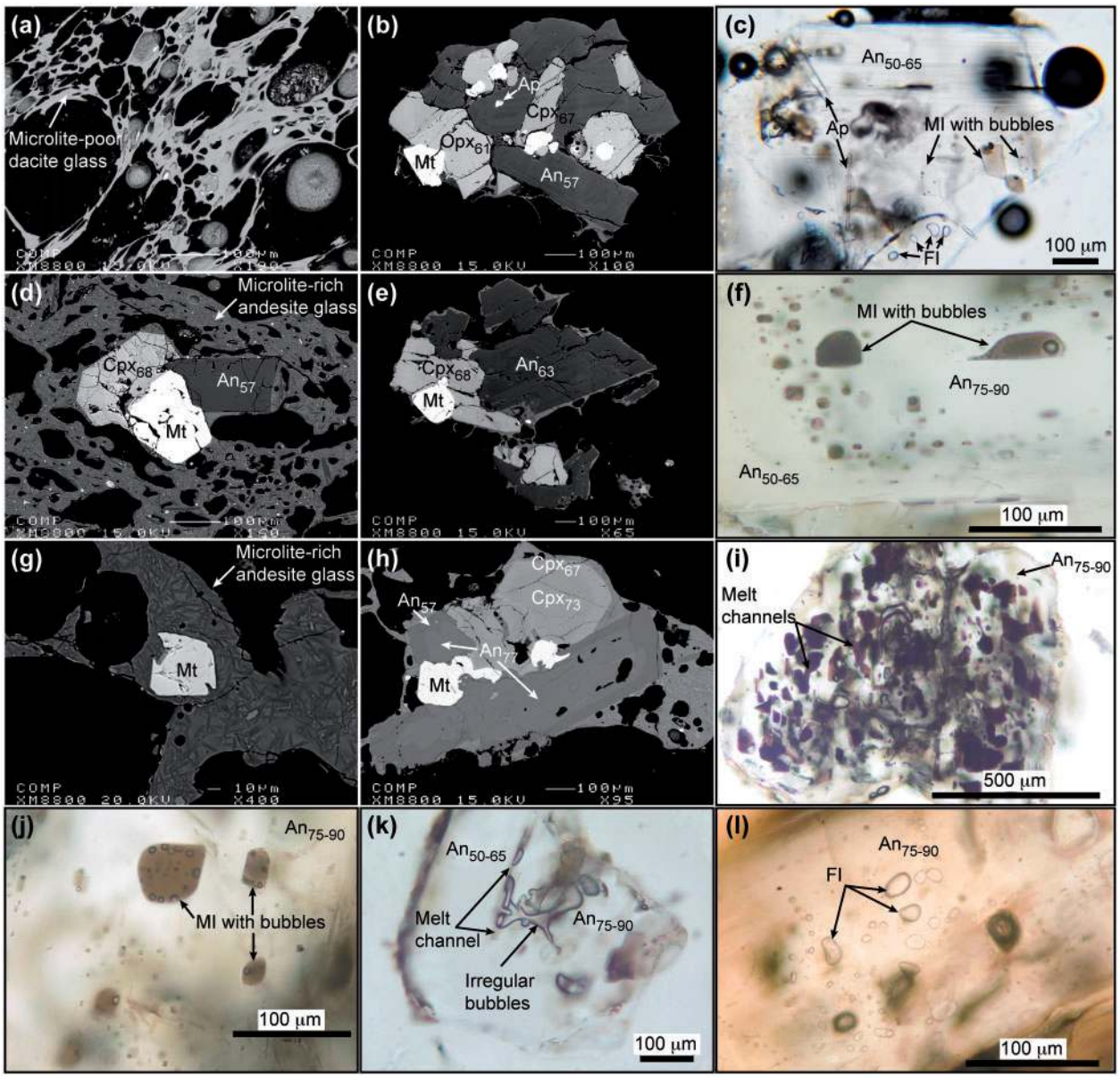

Fig. 3. Mineralogy and textures of the 1835 deposits, illustrated by backscattered electron (BSE) images and photomicrographs. (a) Highly vesicular and microlite-poor glass of the dacite pumice fall. (b) Example of the common glomerocrysts that characterize the dacite mineralogy. The anorthite content of plagioclase and magnesium number of pyroxene are indicated by subscripts. (c) $An_{50–65}$ plagioclase in dacite, showing apatite needles, melt inclusions (MI) featuring bubbles and fluid inclusions (FI). (d) Microlite-rich glass of the silicic andesite scoria fall and glomerocryst of plagioclase, clinopyroxene and titanomagnetite. (e) Glomerocryst found in the silicic andesite, similar to those found in the dacite. Such glomerocrysts are also occasionally found in the andesite scoria. (f) Rimmed, melt-inclusion-bearing calcic plagioclase found in the silicic andesite. (g) Microlite-rich silicic andesite glass of the andesite scoria fall and titanomagnetite microphenocryst. (h) Glomerocrysts showing normal zoning of plagioclase and clinopyroxene in andesite. (i) $An_{75–90}$ phenocryst in andesite showing numerous melt inclusions and melt channels. (j) $An_{75–90}$ plagioclase-hosted, bubble-bearing melt inclusions in andesite. (k) Large, irregular bubbles coexisting with melt (glass) within plagioclase in silicic andesite. (l) Small, rounded and high-relief fluid inclusions within plagioclase in andesite.

characterized by common polyphase glomerocrysts (Fig. 3d and e). However, single phenocrysts of plagioclase are more abundant here than in the dacite and generally host several melt inclusions (Fig. 3f).

The silicic andesite bulk-rock (62·2 wt % SiO_2), matrix glass (60·4–65·6 wt % SiO_2) and melt inclusions (58·3–66·8 wt % SiO_2) show overlapping ranges in silica contents, with essentially identical mean values (Figs 4a

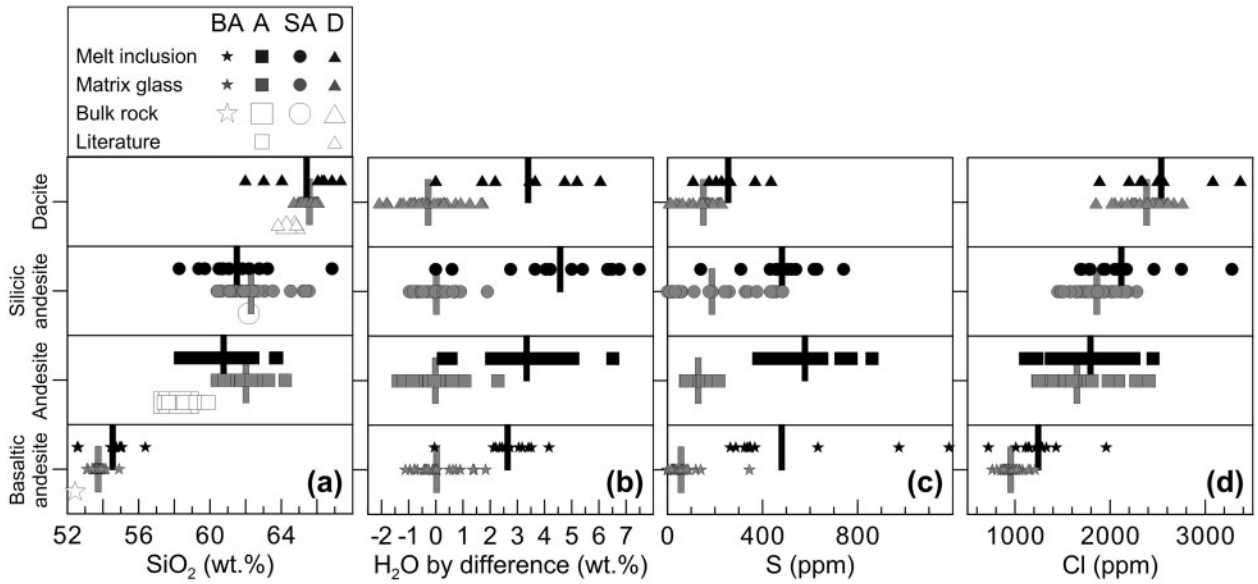

Fig. 4. Ranges in (a) SiO_2, (b) H_2O (volatiles by difference), (c) sulphur and (d) chlorine concentrations for bulk-rocks, matrix glasses and melt inclusions of the dacite (D), silicic andesite (SA), andesite (A) and pre-1835 basaltic andesite (BA). Vertical bars indicate average composition of matrix glasses and melt inclusions. Literature data for bulk-rocks are from Williams (1952), Self *et al.* (1989) and Scott *et al.* (2006).

and 5, Table 1), and similar Al_2O_3 and FeO* contents (Fig. 5c and e). The bulk-rock exhibits higher Sr and V contents than the dacite but lower incompatible trace element concentrations (Fig. 6, Tables 1 and 2). Melt inclusions have higher water (4·6 ± 2·3 wt %), sulphur (480 ± 140 ppm) and chlorine (2120 ± 440 ppm) concentrations than the matrix glass (0·0 ± 0·7 wt % H_2O, 190 ± 180 ppm S, 1860 ± 230 ppm Cl; Fig. 4b–d).

The silicic andesite contains the same plagioclase populations as the dacite, although phenocrysts with an $An_{75–90}$ core now make up about 35% of the feldspars (Figs 3d–f and 7b). Plagioclase microlites have an $An_{49–53}$ composition. Both clinopyroxene and orthopyroxene exhibit two populations based on Mg# (and Al_2O_3), with ranges of 65–70 (Cpx_{67}, low Al_2O_3), 67–73 ($Cpx_{67–73}$, high Al_2O_3), 60–62 (Opx_{61}) and 63–68 ($Opx_{63–68}$) (Fig. 8a and b, Table 3). Crystals of $Cpx_{67–73}$ generally occur as anhedral inclusions within $An_{75–90}$ plagioclase. Magnetite crystals have distinctly lower TiO_2 contents (11·2 wt %) compared with those in the dacite (15·7 wt % TiO_2) (Fig. 8c). Calculated crystallinities of ~3 wt % (2·3 wt % plagioclase, <0·1 wt % clinopyroxene, 0·5 wt % orthopyroxene and <0·1 wt % magnetite; Table 4) agree roughly with the phenocryst-poor nature of the scoria in thin section, but probably underestimate actual values owing to similar bulk-rock and glass compositions.

Andesite

The andesite scoria consists of moderately vesicular, microlite-rich glass, abundant phenocrysts of plagioclase and sparse clinopyroxene, orthopyroxene and magnetite occurring as single crystals or scarcer glomerocrysts (Fig. 3g–i). Apatite is absent. Abundant plagioclase-hosted melt inclusions commonly feature several small bubbles (Fig. 3j). Like the dacite, the andesite is characterized by the occurrence of small H_2O-rich fluid inclusions and iron sulphide globules hosted in phenocrysts (Fig. 3k and l). Two out of three sulphide inclusions analysed in the andesite contain ~28 wt % Cu.

Andesite bulk-rocks show lower silica (57·4–58·8 wt % SiO_2) than the matrix glass (60·4–64·2 wt % SiO_2), the latter being essentially identical to the silicic andesite glass. The silica content of the melt inclusions (58·3–63·8 wt % SiO_2) overlaps with that of the bulk-rocks but extends to higher values (Figs 4a and 5, Table 1). At a given SiO_2, bulk-rocks have higher Al_2O_3 and lower FeO* compared with melt inclusions (Fig. 5c and e). The andesite bulk-rocks are enriched in Sr and V and depleted in K, Rb, Zr, Ba and the REE compared with the dacite and silicic andesite (Fig. 6, Tables 1 and 2). The REE pattern for the andesite is parallel to that of the dacite, with a smaller negative Eu anomaly (Fig. 6d). Melt inclusions have higher water (3·3 ± 1·7 wt %), sulphur (580 ± 120 ppm) and chlorine (1790 ± 330 ppm) concentrations than matrix glass (0·0 ± 0·8 wt % H_2O, 130 ± 40 ppm S, 1650 ± 350 ppm Cl; Fig. 4b–d).

Phenocryst populations in the andesite are significantly different from those in the dacite and silicic andesite. Here $An_{50–65}$ plagioclase represents only ~10% of the feldspars, generally occurring in subhedral polyphase glomerocrysts and displaying weak oscillatory zoning.

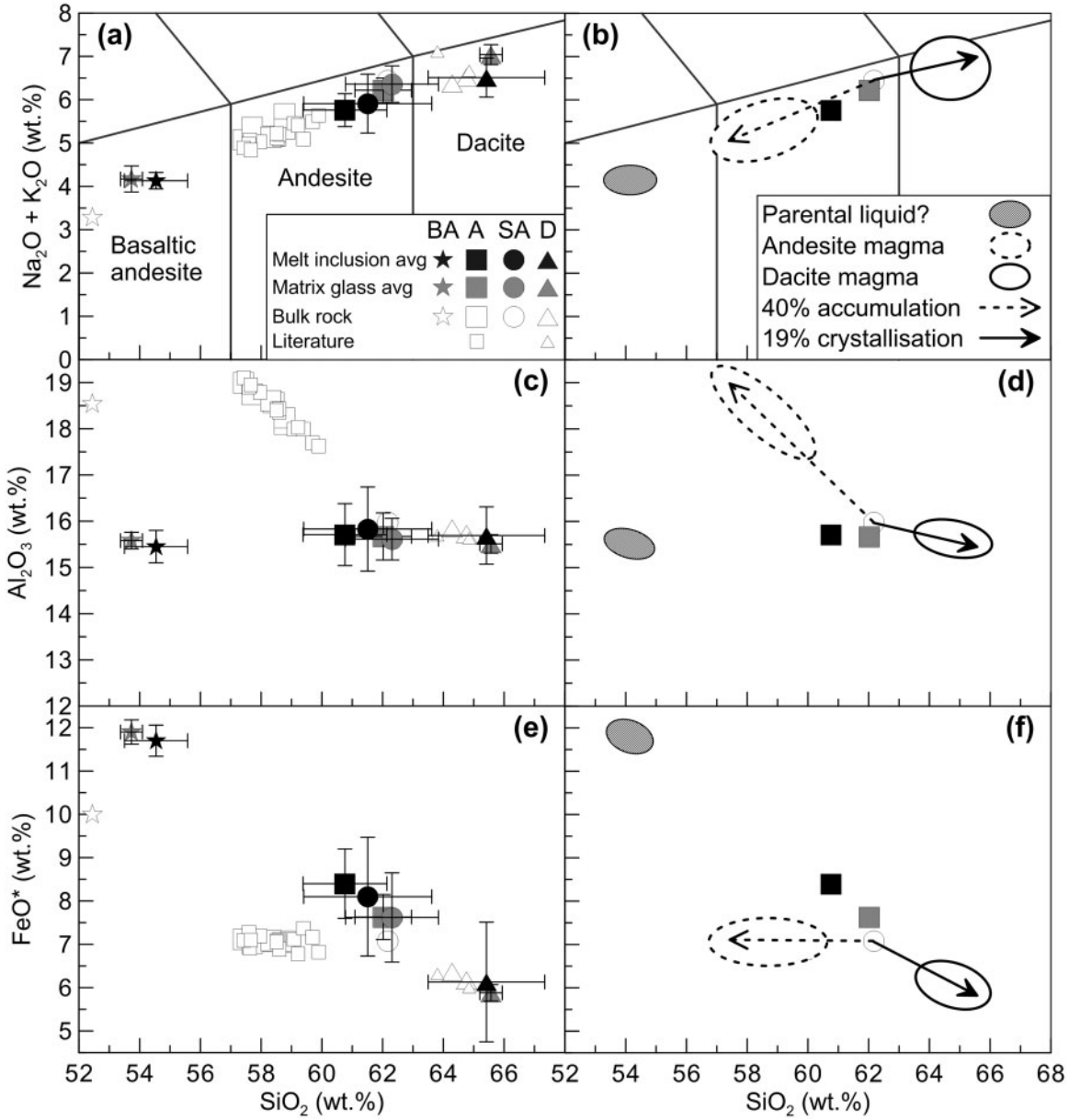

Fig. 5. (a, c, e) $Na_2O + K_2O$, Al_2O_3 and FeO* contents as a function of SiO_2 for bulk-rocks, matrix glasses and melt inclusions. Whereas a linear trend is observed for $Na_2O + K_2O$ (a), andesite bulk-rocks fall off the liquid line of descent defined by all matrix glasses and melt inclusions, as well as by silicic andesite and dacite bulk-rocks. This indicates that the andesite bulk-rocks do not represent true melts, but instead mixtures of silicic andesite melt and accumulated (dominantly plagioclase) crystals. (b, d, f) Results of mass-balance calculations that reproduce the andesite bulk-rock compositional range from the silicic andesite bulk-rock by addition of up to 40% of a mineral assemblage similar to that found in the andesite scoria. In addition, the dacite glass (most evolved liquid) can be derived from the silicic andesite by ~19% fractional crystallization of a mineral assemblage similar to that found in the silicic andesite and dacite.

Approximately 80% of the feldspars in the andesite are $An_{75–90}$ plagioclase that commonly exhibits a sieve texture with numerous melt inclusions and frequent melt channels, indicative of partial dissolution (Figs 3h, i and 7c). About 15% of the $An_{75–90}$ crystals have a thin overgrowth rim of $An_{50–65}$; this zoning is similar to that observed in the dacite and silicic andesite. A third population, comprising ~10% of the plagioclase phenocrysts, is characterized by a highly calcic composition ($An_{90–95}$) and sieve texture. By contrast, the plagioclase microlites are $An_{53–57}$. Clinopyroxene and orthopyroxene populations overlap with those of the silicic andesite, with Mg# ranges of 64–70 (Cpx_{67}, low Al_2O_3), 67–75 ($Cpx_{67–75}$, high Al_2O_3), 59–62 (Opx_{61}) and 64–72 ($Opx_{64–72}$) (Fig. 8a and b, Table 3). Again, $Cpx_{67–75}$ occurs almost exclusively as anhedral crystals and as inclusions within

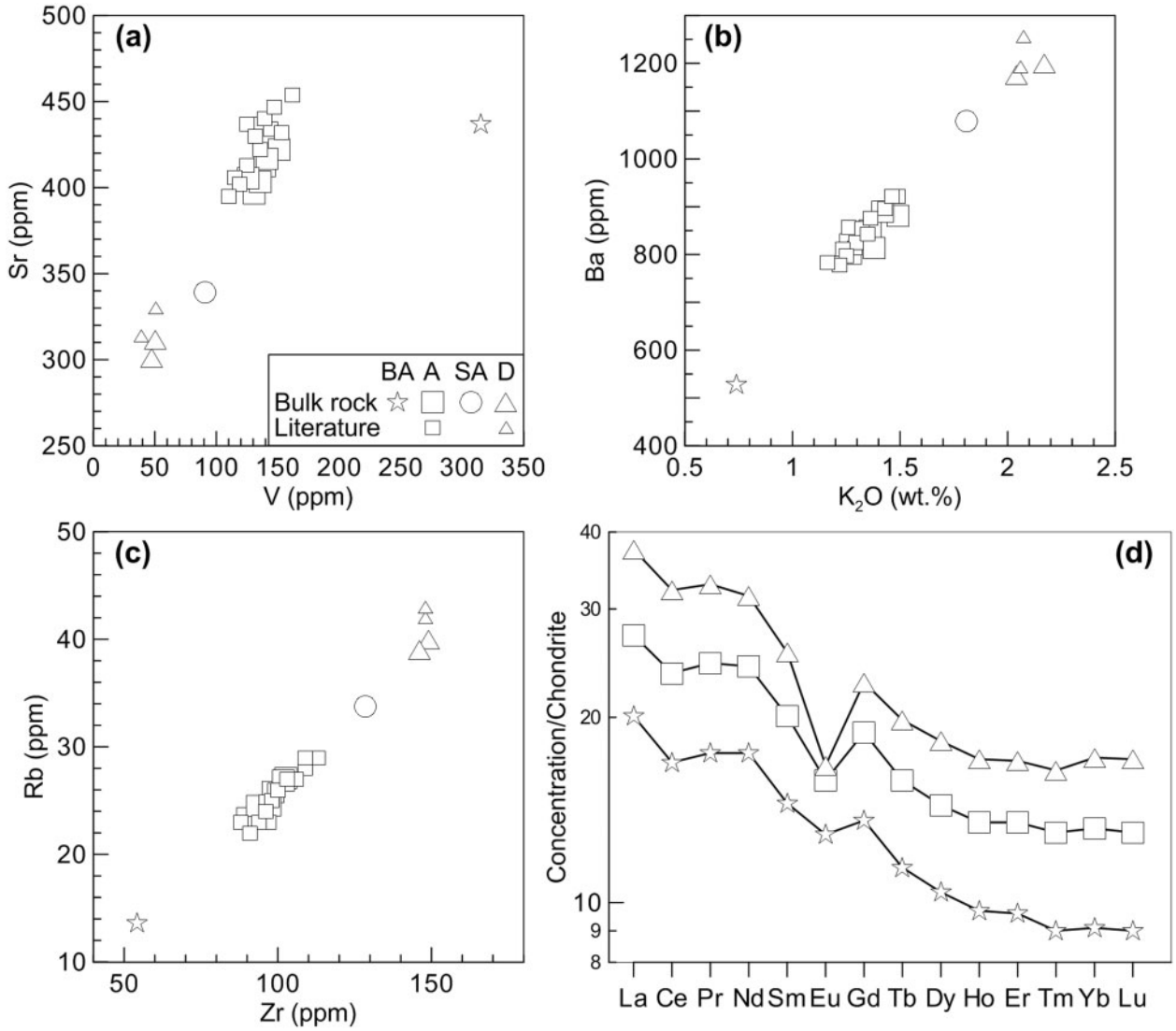

Fig. 6. Trace element composition of Cosigüina bulk-rock samples. (a) Depletion in the compatible elements Sr and V from basaltic andesite to dacite. Although the andesite has Sr contents similar to that of the pre-1835 basaltic andesite, its V concentration is about half that of the basaltic andesite. This may be due to plagioclase accumulation in the andesite. (b, c) Systematic enrichment in incompatible elements K, Rb, Zr and Ba from basaltic andesite to dacite. (d) Chondrite-normalized (Boynton, 1984) REE patterns for dacite, andesite and basaltic andesite, showing parallel patterns, enrichment in all REE and increasingly negative Eu anomalies from basaltic andesite to dacite. We also note the occurrence of negative Ce anomalies in the Cosigüina rocks. Such Ce anomalies also have been observed at other localities in Nicaragua (e.g. Kutterolf *et al.*, 2011), and are probably related to the input and composition of sediments in the subduction zone (e.g. Hole *et al.*, 1984; Plank & Langmuir, 1998).

$An_{75–90}$ plagioclase. Rare magnetite crystals display a wide range of TiO_2 contents, from 7·6 to 14·6 wt % (Fig. 8c). Calculated crystal contents range from 12·8 wt % plagioclase, 1·8 wt % clinopyroxene, 0·1 wt % orthopyroxene and 0·2 wt % magnetite for the least mafic bulk andesite (total of 15 wt %) to 23·6 wt % plagioclase, 2·7 wt % clinopyroxene, 1·3 wt % orthopyroxene and 1·4 wt % magnetite for the most mafic sample (total of 29 wt %; Table 4). For comparison, five modal analyses on andesite scoria samples by Self *et al.* (1989) gave 20·1–23·4 vol. % (21·2–24·6 wt %) plagioclase, 0·9–1·0 vol. % (1·2–1·3 wt %) clinopyroxene, 0·2–0·3 vol. % (0·3–0·4 wt %) orthopyroxene and 0·4–0·5 vol. % (0·8–1·0 wt %) magnetite.

Pre-1835 basaltic andesite

The pre-1835 basaltic andesite scoria is composed of vesicular, microlite-poor dark glass and abundant phenocrysts of plagioclase and olivine with lesser amounts of pyroxene and Fe–Ti oxides. Melt inclusions are widespread and commonly show bubbles.

Table 2: Rare earth element compositions (in ppm) of representative samples of 1835 dacite and andesite and pre-1835 basaltic andesite bulk-rocks analysed by ICP-MS

Name:	COS-A-1	COS-M-50	COS-H-36
Deposit:	Pumice fall	Scoria fall	Scoria fall
Analysis:	Dacite bulk	Andesite bulk	Basaltic andesite bulk
Locality:	1	2	3
La	11·63	8·42	6·23
Ce	26·00	19·05	13·65
Pr	4·01	2·99	2·13
Nd	18·92	14·49	10·49
Sm	4·98	3·91	2·83
Eu	1·23	1·16	0·95
Gd	5·91	4·89	3·52
Tb	0·94	0·75	0·54
Dy	5·90	4·64	3·35
Ho	1·23	0·97	0·70
Er	3·57	2·84	2·01
Tm	0·53	0·42	0·29
Yb	3·59	2·76	1·91
Lu	0·55	0·42	0·29

The basaltic andesite bulk-rock is among Cosigüina's most mafic documented samples (52·4 wt % SiO_2, 4·5 wt % MgO), with slightly more silicic matrix glass (53·1–54·9 wt % SiO_2, 4·4–4·8 wt % MgO) and melt inclusions (52·6–56·4 wt % SiO_2, 3·5–5·5 wt % MgO) (Figs 4a and 5, Table 1). Similar to the andesite, the basaltic andesite bulk-rock has higher Al_2O_3 and lower FeO* than the matrix glass and melt inclusions (Fig. 5c and e). The basaltic andesite exhibits the highest compatible trace element concentrations, although its Sr content is similar to that of the andesite, and the lowest incompatible element concentrations among the analysed bulk-rocks (Fig. 6, Tables 1 and 2). Its REE pattern displays a subdued negative Eu anomaly (Fig. 6d). Here again, melt inclusions show higher water ($2·6 \pm 1·0$ wt %), sulphur (480 ± 300 ppm) and chlorine (1240 ± 290 ppm) concentrations than matrix glass ($0·0 \pm 0·8$ wt % H_2O, 60 ± 70 ppm S, 960 ± 110 ppm Cl, Fig. 4b–d).

Plagioclase phenocrysts in the basaltic andesite are characterized by a compositional range of $An_{75–95}$, similar to that of the dominant population in the 1835 andesite (Fig. 7d). Phenocrysts commonly display a sieve texture associated with melt inclusions and melt channels. Microlites are $An_{54–58}$ plagioclase. Analyses on four olivine phenocrysts give compositions in the range $Fo_{71–74}$ [$Fo = 100 \times$ molar $Mg/(Mg + Fe_{total})$] with no apparent core-to-rim zonation (Table 3). Mass-balance calculations indicate a crystal content of 20 wt % (18·0 wt % plagioclase, 2·2 wt % olivine, 0·1 wt % clinopyroxene, and <0·1 wt % magnetite; Table 4).

Magmatic conditions and magma properties

Equilibrium minerals, liquids, and magma temperatures

The composition of coexisting minerals and liquid, if in chemical equilibrium, can be used to calculate magma temperatures. Here we assess equilibrium between pyroxene–liquid and clinopyroxene–orthopyroxene pairs based on Fe–Mg exchange coefficients and use MELTS calculations of fractional crystallization sequences (Ghiorso & Sack, 1995) to test mineral–liquid associations, including plagioclase–liquid pairs. We then apply thermometers based on clinopyroxene–liquid (Putirka *et al.*, 2003) and two-pyroxene [Putirka, 2008, equation (36)] equilibria as well as apatite saturation (Harrison & Watson, 1984), whose expressions are independent of the H_2O content of the liquid, to estimate the pre-eruptive temperature of the 1835 magmas. We also use olivine–liquid thermometry [Putirka, 2008, equation (22)] to estimate the temperature of the pre-1835 basaltic andesite.

For clinopyroxene–liquid equilibrium, the expected $K_D(Fe–Mg)^{cpx–liq}$ value is $0·28 \pm 0·08$ (Putirka, 2008). This would imply that Cpx_{67}, present in all 1835 samples, is probably derived from an andesite liquid [observed $K_D(Fe–Mg)^{cpx–liq}$ of 0·25–0·28] rather than from dacite [observed $K_D(Fe–Mg)^{cpx–liq}$ of 0·17]. However, MELTS simulations indicate crystallization of this clinopyroxene composition over a range of melt SiO_2 contents and temperatures, spanning andesitic to dacitic compositions (Supplementary Data Fig. A2). Using Cpx_{67}–dacite glass and Cpx_{67}–average andesite melt inclusion pairs, the clinopyroxene–liquid thermometer of Putirka *et al.* (2003) yields temperatures of ~930°C and ~1010°C for the dacite and andesite, respectively. In turn, high-Al_2O_3 $Cpx_{67–75}$, commonly found as anhedral crystals and inclusions in calcic plagioclase, must be derived from a more mafic liquid, and would be in Fe–Mg equilibrium with the most mafic melt inclusion [MgO = 5·5 wt %, observed $K_D(Fe–Mg)^{cpx–liq}$ of 0·27] found in the pre-1835 basaltic andesite. This is supported by MELTS models, which do not produce magnesian clinopyroxene at the conditions tested. The high-Al_2O_3 $Cpx_{67–75}$ crystals may thus be 'antecrysts' in the 1835 andesite and originate from an earlier stage of differentiation at higher temperature. The $Cpx_{67–75}$–basaltic andesite melt inclusion pair gives a temperature of 1120°C, in agreement with olivine–liquid thermometry of 1110–1170°C for the basaltic andesite (Fig. 9a).

For orthopyroxene–liquid equilibrium, the expected $K_D(Fe–Mg)^{opx–liq}$ is $0·29 \pm 0·06$, but decreases slightly with increasing liquid SiO_2 content according to K_D(Fe–

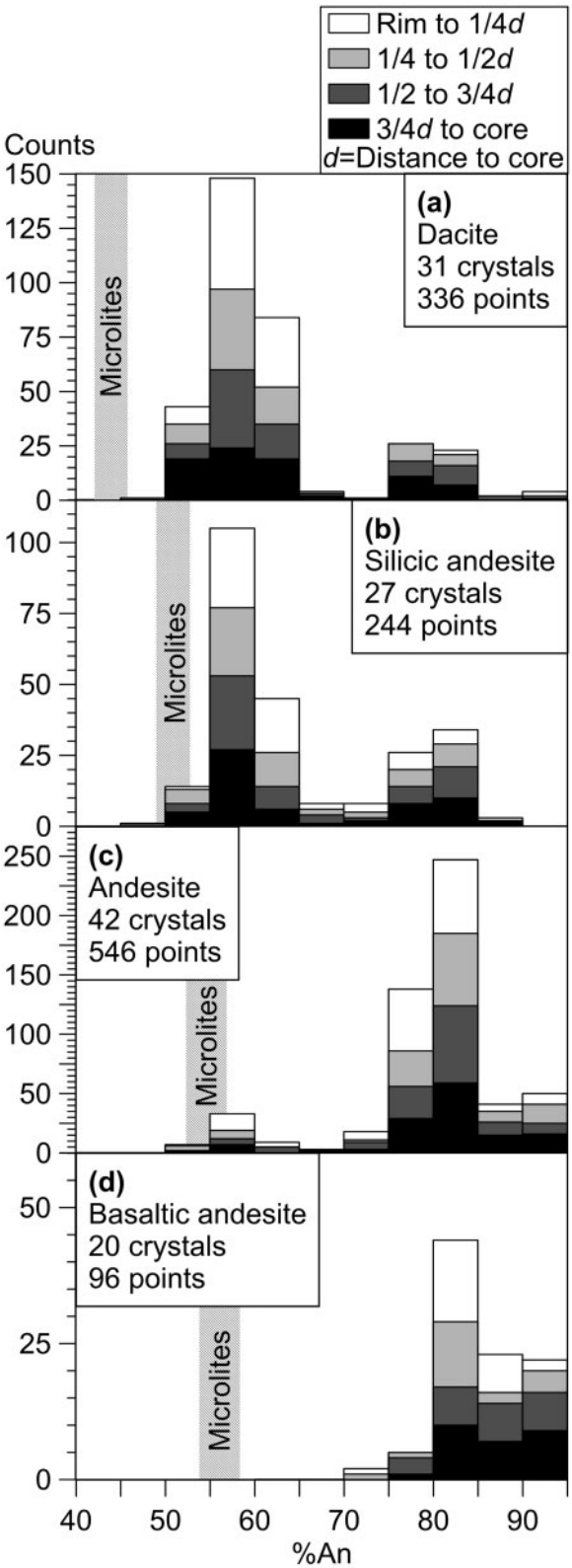

Fig. 7. Cumulative histograms showing the composition of plagioclase phenocrysts in (a) dacite, (b) silicic andesite, (c) andesite from 1835 and (d) pre-1835 basaltic andesite. The shading in the stacked bars indicates the relative position of analyses along core-to-rim traverses (see key). Three plagioclase phenocryst populations, $An_{50–65}$, $An_{75–90}$ and $An_{90–95}$, are observed in the 1835 eruptive products, whereas the pre-1835 basaltic andesite contains $An_{75–95}$ plagioclase. Data from detailed plagioclase traverses (Fig. 11) are not included in these plots. Shaded bars indicate the composition of microlites in each sample.

$Mg)^{opx–liq} = 0{\cdot}4805 - 0.3733 \times X_{Si}^{liq}$, where X_{Si}^{liq} is the cation fraction of SiO_2 in the liquid (Putirka, 2008). This results in expected K_D values of 0·25 for the dacite glass and 0·27 for the average andesite melt inclusion composition. Observed K_D values for Opx_{61}–dacite glass and $Opx_{63–72}$–andesite melt inclusion pairs are thus within error of equilibrium, at 0·23 and 0·26, respectively. MELTS calculations are consistent with bimodal orthopyroxene populations and the associations of Opx_{61} with dacite and $Opx_{63–72}$ with andesite.

The above analysis suggests that Cpx_{67} and $Opx_{63–72}$ were coeval and should be in equilibrium with each other, as confirmed by a $K_D(Fe–Mg)^{cpx–opx} = 1{\cdot}08$, close to the expected value of $1{\cdot}09 \pm 0{\cdot}14$ (Putirka, 2008). In the pressure range 0·01–1000 MPa, the two-pyroxene thermometer results in a temperature range of 960–1010°C (Fig. 9a), consistent with the clinopyroxene–liquid results for the andesite.

Equilibrium between plagioclase and melt is strongly affected by the H_2O content of the melt and is thus used in a later section as a hygrometer. Nevertheless, it is noteworthy that MELTS models, considering reasonable melt H_2O contents as inputs, do not produce plagioclase as calcic as the $An_{75–95}$ crystals hosted in the andesite and basaltic andesite (Supplementary Data Fig. A2). In contrast, the models are consistent with $An_{50–65}$ plagioclase being derived from silicic andesite to dacite liquids over the temperature range obtained by clinopyroxene–melt and two-pyroxene thermometry. Subsequent application of the hygrometer of Lange *et al.* (2009) and Mg partitioning (Bindeman *et al.*, 1998) places further constraints on plagioclase–liquid associations.

Additional independent constraints on the temperature of the Cosigüina magmas can be obtained from the apatite saturation model of Harrison & Watson (1984), which depends only on the concentrations of SiO_2 and P_2O_5 in the liquid (P_2O_5 concentration in apatite being near-invariant). According to this model, the lack of apatite in the andesite indicates temperatures in excess of 930°C, consistent with the above results. In contrast, the occurrence of apatite in the dacite, together with its higher SiO_2 and P_2O_5, implies a temperature equal to or lower than ~950°C.

To summarize, mineral–liquid Fe–Mg exchange coefficients and MELTS simulations suggest that calcic $An_{75–90}$ plagioclase and high-Al_2O_3 $Cpx_{67–75}$ represent cognate

Table 3: Representative compositions (wt %) of plagioclase, clinopyroxene, orthopyroxene, magnetite, apatite and olivine populations from Cosigüina tephras

Mineral:	Plagioclase		Apatite	Clinopyroxene		Olivine	Magnetite		Orthopyroxene	
Population:	An_{50-65}	An_{75-90}	Ap	Cpx_{67}	Cpx_{67-75}	Fo_{71-74}	Mt_{16}	Mt_{8-15}	Opx_{61}	Opx_{63-72}
SiO_2	53·82	47·80	0·23	51·00	51·04	38·22	0·03	0·08	52·18	53·07
TiO_2	0·03	0·02	–	0·45	0·46	0·01	15·66	10·76	0·25	0·24
Al_2O_3	28·78	32·66	–	1·68	2·07	0·01	2·91	3·97	0·86	1·09
FeO*	0·49	0·69	0·76	12·25	10·18	24·78	75·49	77·12	23·96	19·43
MnO	–	–	0·12	0·52	0·39	0·43	0·57	0·44	0·89	0·67
MgO	0·06	0·07	0·24	14·07	15·12	36·94	2·16	2·93	20·62	23·72
CaO	11·75	16·39	54·24	19·44	19·87	0·20	0·02	0·06	1·71	1·70
Na_2O	4·56	2·01	0·03	0·25	0·27	0·00	–	–	0·02	0·04
K_2O	0·18	0·06	–	0·02	0·02	–	–	–	0·02	0·03
P_2O_5	–	–	41·78	–	–	–	–	–	–	–
Total	99·67	99·70	97·40	99·69	99·43	100·59	96·84	95·36	100·52	99·97
F	–	–	1·69	–	–	–	–	–	–	–
Cl	–	–	0·88	–	–	–	–	–	–	–
S	–	–	b.d.l.	–	–	–	–	–	–	–

*Fe reported as FeO.

Table 4: Results of least-squares mass-balance calculations

Model:	1	2	3	4	5	6	7
Initial magma:	Dacite bulk	Silicic andesite bulk	Andesite bulk*	Andesite bulk†	Basaltic andesite bulk	Silicic andesite bulk	Silicic andesite bulk
Final magma:	Dacite glass	Silicic andesite glass	Andesite glass	Andesite glass	Basaltic andesite glass	Andesite bulk†	Dacite glass
An_{50-65}	–4·6	–2·3	–	–	–	–	–11·6
An_{75-90}	–	–	–12·8	–23·6	–18·0	33·2	–
Ap	–0·1	–	–	–	–	–	–0·4
Cpx_{67}	–0·5	∼0	–	–	–	–	–1·6
Cpx_{67-75}	–	–	–1·8	–2·7	–0·1	3·8	–
Fo_{71-74}	–	–	–	–	–2·2	–	
Mt_{16}	–0·6	∼0	–	–	–	–	–1·7
Mt_{8-15}	–	–	–0·2	–1·4	∼0	2·2	–
Opx_{61}	–1·4	–0·5	–	–	–	–	–3·4
Opx_{63-72}	–	–	–0·1	–1·3	–	3·0	–
$R^{2‡}$	0·15	0·07	0·29	0·23	0·12	0·01	0·04
Crystallinity (wt %/vol. %)	7/6	3/2	15/14	29/26	20/20	–	–

*Least mafic andesite scoria, sample 15 of Scott *et al*. (2006).
†Most mafic andesite scoria, sample COS-A-5.
‡Sum of the squares of the residuals from the calculations.
Numbers are amounts, as wt % of initial magma, of phases added or subtracted to the initial magma to reproduce the final magma composition.

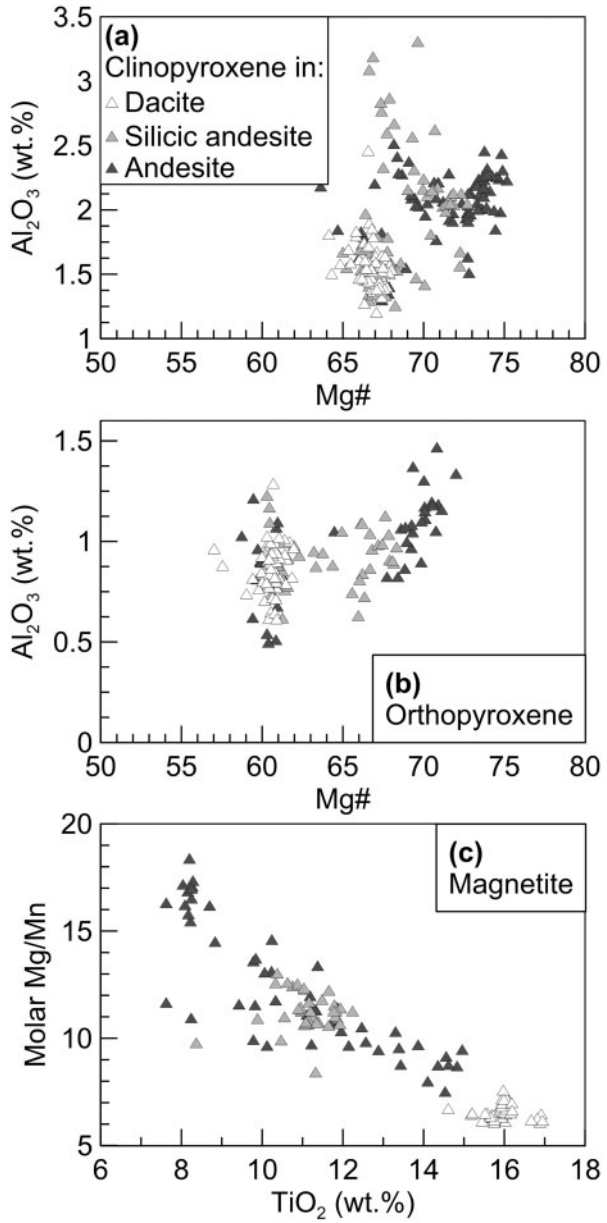

Fig. 8. Composition of (a) clinopyroxene, (b) orthopyroxene and (c) magnetite phenocrysts from the 1835 deposits. Both clinopyroxene and orthopyroxene are present in two populations: low-Al_2O_3 Cpx_{67} and high-Al_2O_3 $Cpx_{67–75}$; Opx_{61} and $Opx_{63–72}$. Magnetites show distinct compositions, best expressed by their TiO_2 content, in each of the 1835 samples. Number of crystals analysed/total number of microprobe analyses for dacite, silicic andesite and andesite, respectively, are: (a) 17/91, 13/67, 13/79; (b) 14/74, 13/52, 12/50; (c) 24/42, 23/38, 35/52.

crystals forming at high temperature from mafic basaltic andesite. Low-Al_2O_3 Cpx_{67}, $Opx_{63–72}$ and $An_{50–65}$ plagioclase formed from andesitic to dacitic liquids in the temperature range of 930–1010°C. Crystals of Opx_{61} and apatite probably crystallized only from dacite at a temperature ≤950°C according to apatite saturation constraints.

Oxygen fugacity

Two-oxide thermobarometry (e.g. Ghiorso & Evans, 2008) is commonly used to constrain the temperature and oxygen fugacity (fO_2) of silicic magmas (e.g. Devine *et al.*, 2003). We could not apply this technique here, however, because of the lack of ilmenite in the 1835 samples. Rough estimates of fO_2 conditions were obtained using the approach of France *et al.* (2010), which is based on the FeO content of coexisting clinopyroxene and plagioclase phenocrysts and the composition of the liquid. Assuming equilibrium of Cpx_{67} and $An_{50–65}$ with andesite to dacite liquids in the temperature range 930–1010°C, this method suggests log fO_2 of $\Delta NNO = -0{\cdot}5 \pm 0{\cdot}3$ (1σ) ($\Delta NNO = \log fO_2$ of the sample − log fO_2 at the nickel–nickel oxide buffer). We note, however, that this method may not be optimal for the silicic Cosigüina magmas as it is calibrated only for liquid compositions with $SiO_2 < 60$ wt %. Notably, using $Cpx_{67–75}$ and $An_{75–90}$ with mafic basaltic andesite liquid at 1110°C yields $\Delta NNO = 0{\cdot}8 \pm 0{\cdot}6$. In comparison, the expression of Kilinc *et al.* (1983) suggests more oxidizing conditions overall ($\Delta NNO = 0–1{\cdot}5$) at Cosigüina, assuming an $Fe^{3+}/\Sigma Fe$ range of 0·18–0·32 typical for subduction zone magmas (Kelley & Cottrell, 2009). Martel *et al.* (1999) have shown that fO_2 exerts strong control on the Ti content of magnetite crystallizing from andesitic magma (see also Frost & Lindsley, 1991). Their experiments on Mont Pelée andesite, which has a composition close to the Cosigüina andesite, produced magnetite but no ilmenite at $\Delta NNO > 0$. Comparing Cosigüina magnetites with the experimental data of Martel *et al.* (1999) suggests that the 1835 magmas had an fO_2 in the range $\Delta NNO = 0–1$ (Fig. 9b). This appears to be our most robust estimate of oxygen fugacity conditions in the 1835 magma reservoir. Interestingly, the increasing Ti content of magnetite from andesite to dacite (Figs 8c and 9b) may indicate reduction of the magma's oxidation state during differentiation (e.g. Kelley & Cottrell, 2012).

H_2O contents of the magmas

The dissolved water concentration in magmas, and whether or not a particular magmatic system has reached saturation with an H_2O-rich vapour phase, has profound implications for phase relations, magma properties and the style of potential volcanic eruptions. Our approach to estimate the pre-eruptive water contents of the Cosigüina magmas is based on indirect measurements using the volatiles-by-difference method and a comparison with the results of plagioclase–melt hygrometry (Putirka, 2008; Lange *et al.*, 2009). The hygrometers are highly sensitive to temperature (pressure has a weak effect) and are therefore best applied with temperature estimated independently.

As detailed in the analytical methods section (see also Supplementary Data Fig. A1), the accuracy of our volatiles-by-difference method appears suitable for

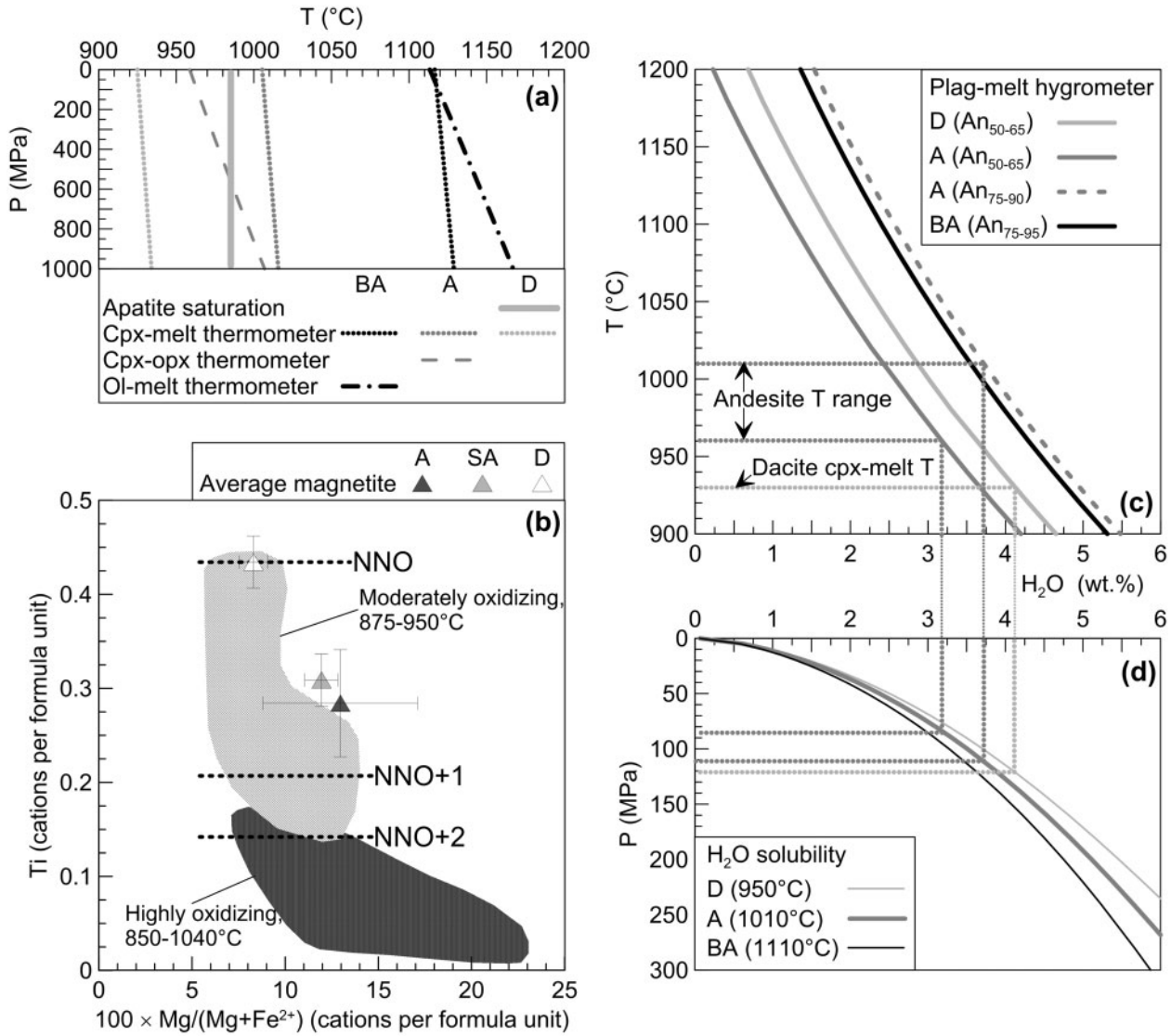

Fig. 9. Thermobarometric and hygrometric estimates of magma reservoir conditions. (a) Whereas apatite saturation in dacite implies a temperature ≤950°C (Harrison & Watson, 1984), pressure-sensitive thermometers based on clinopyroxene–melt equilibrium (Putirka *et al.*, 2003) and two-pyroxene equilibrium [Putirka, 2008, equation (36)] suggest 930°C for dacite and 960–1010°C for andesite. In addition, clinopyroxene–melt and olivine–melt equilibria [Putirka, 2008, equation (22)] indicate temperatures in the range of 1110–1170°C for basaltic andesite. (b) Estimate of fO_2 conditions based on a comparison of magnetite composition in the Cosigüina samples and in products of fO_2-controlled experiments on Mont Pelée andesite (Martel *et al.*, 1999). Magnetite composition is reported in cations per formula unit (total of three cations and four oxygens) (e.g. Andersen *et al.*, 1993). Triangles are average magnetite compositions (±1σ) at Cosigüina and fields show the compositional range of experimental magnetites at the given temperature–fO_2 conditions. The Ti content of magnetite is a strong function of fO_2 in the experiments (ilmenite is not present), suggesting fO_2 conditions of ΔNNO = 0–1 for the Cosigüina magmas. (c) The plagioclase–melt hygrometer of Lange *et al.* (2009). Curves for $An_{50–65}$–dacite glass, $An_{50–65}$–andesite glass, $An_{75–90}$–andesite melt inclusions and $An_{75–95}$–basaltic andesite glass pairs at 0·1 MPa show the strong temperature dependence of the hygrometer. The range of temperatures derived for the dacite and andesite in (a) are projected to the 0·1 MPa curves and yield minimum water contents of 3·2–4·2 wt % for the 1835 magmas. (d) Assuming H_2O saturation, water estimates from (c) are used to infer a minimum magma reservoir pressure of ~100 MPa, using the solubility model of Moore *et al.* (1998).

intermediate water contents (3·6 wt % H_2O by difference compared with 3·95 wt % H_2O by ion microprobe for the M3N standard) and is better than 0·9 wt % H_2O overall. Results for the Cosigüina melt inclusions yield average (± 1σ) dissolved water contents of 3·4 ± 1·9 wt % for dacite, 4·6 ± 2·3 wt % for silicic andesite, 3·3 ± 1·7 wt % for andesite and 2·6 ± 1·0 wt % for the pre-1835 basaltic andesite (Fig. 4b). In comparison, assuming $An_{50–65}$ plagioclase in equilibrium with andesite to dacite liquids and the temperature range 930–960°C derived from mineral–melt

thermometry, the plagioclase–melt hygrometer of Lange *et al.* (2009) yields minimum (at 1 bar) melt H_2O contents of 3·2–4·2 wt %, in close agreement with our volatiles-by-difference results (Fig. 9c). Contrasting with MELTS results, the hygrometer also suggests that, at a temperature of 1010°C, $An_{75–90}$ plagioclase could indeed crystallize from the andesite (melt inclusion composition) if it had 3·7–3·8 wt % dissolved H_2O. In addition, we find that the pre-1835 basaltic andesite may be in equilibrium with its observed $An_{75–95}$ phenocryst population at 1110–1170°C and 2–2·5 wt % dissolved H_2O. In comparison with the phenocrysts, plagioclase microlites have systematically lower anorthite contents (Fig. 7); this is consistent with microlite formation during syn-eruptive degassing and lowered melt H_2O contents. The modest water contents inferred here are consistent with the absence of amphibole as a phenocryst phase in the 1835 products, and at Cosigüina in general. Phase equilibria experiments on similar andesitic to dacitic bulk compositions stabilize amphibole for comparatively high water contents and/or low-temperature and/or high-pressure conditions (Rutherford & Devine, 1988; Barclay *et al.*, 1998; Martel *et al.*, 1999; Pichavant *et al.*, 2002; Costa *et al.*, 2004).

The occurrence of phenocryst-hosted H_2O-rich fluid inclusions demonstrates that the 1835 magmas coexisted with an H_2O-rich vapour prior to eruption (T. Hansteen, personal communication; Longpré *et al.*, in preparation). Of the ubiquitous bubbles present in the melt inclusions, some may represent a magmatic gas phase that was present during entrapment rather than post-entrapment melt shrinkage during cooling (e.g. Lowenstern, 1993). This is also consistent with our volatiles-by-difference results. The precision of our water estimates is better than $\pm 0{\cdot}8$ wt % (1σ), based on repeated analyses of hydrous glass standards. Standard deviations ($\sigma \geq 1{\cdot}7$ wt %) for melt inclusion results for the 1835 samples exceed this precision level, suggesting that the obtained ranges reflect, at least in part, actual differences in water content rather than scattering about a single value. The results for matrix glasses, which scatter about zero with standard deviations ($\sigma \leq 1{\cdot}0$ wt %) lower than those for melt inclusions, also suggest variable water contents in the melt inclusions (Fig. 4b). We interpret this to reflect melt inclusion entrapment as the andesite to dacite liquids underwent variable extents of magmatic degassing.

Pressure of magma storage

Standard errors for temperature-sensitive barometers based on pyroxene–melt and plagioclase–melt equilibria are of the order of 150–200 MPa based on calibration data (Putirka *et al.*, 2003; Putirka, 2005) and somewhat higher for global experimental datasets (Putirka, 2008). These limitations may be problematic for low-pressure magmatic systems; for example, in the present case, the barometers largely yield negative pressure estimates.

Minimum estimates of magma storage pressure can be derived from dissolved water concentrations determined in the previous section, assuming H_2O saturation in the magma. The model of Moore *et al.* (1998) for H_2O solubility indicates a pressure of the order of 100 MPa for the 1835 magma reservoir, corresponding to an approximate depth of 4 km beneath Cosigüina (Fig. 9d). Such a shallow magma reservoir is in agreement with microthermometry work on the H_2O-rich fluid inclusions, in which a minor CO_2 component is detectable, indicating an essentially identical pressure (T. Hansteen, personal communication; Longpré *et al.*, in preparation). However, if significant amounts of CO_2 also remained dissolved in the magma, higher pressures would be obtained (e.g. Papale, 1999).

Magma density and viscosity

We calculated the density of the 1835 magmatic liquids using the method of Spera (2000), assuming 3·4 and 3·3 wt % dissolved H_2O and temperatures of 950 and 1010°C for the dacite and andesite, respectively, at a pressure of 100 MPa. The results are consistent with the andesite liquid being slightly denser, at $\sim 2500\ \mathrm{kg\ m^{-3}}$, than the dacite melt with $\rho \approx 2400\ \mathrm{kg\ m^{-3}}$. Adding observed mineral assemblages (dominated by plagioclase) has a negligible effect on magma density. However, the presence of gas bubbles in either the andesite or dacite would drastically reduce magma density.

Melt viscosity can in turn be estimated using the model of Giordano *et al.* (2008). Using the same dissolved water and temperature constraints as for the density calculations above, we obtained values of 4×10^3 and 8×10^2 Pa s for the dacite and andesite liquids, respectively. The presence of suspended crystals in the magma (up to ~30 wt % for the andesite based on mass balance) acts as an efficient stiffener. This effect can be crudely approximated with the Einstein–Roscoe equation (e.g. Roscoe, 1952)

$$\eta_{\mathrm{eff}} = \eta_{\mathrm{melt}}(1 - \phi/\omega)^{-2.5}$$

where η_{eff} is the effective viscosity of the magma, η_{melt} is the viscosity of the melt fraction, ϕ is the solid fraction present in the magma and ω is a critical solid fraction beyond which the magma is believed to behave as a solid. In his study of Aleutian lavas, Marsh (1981) determined that this critical crystallinity is about ~55% for basalts, decreases with increasing silica content and may be as low as ~25% for andesites. For solid fractions of 0·06 and 0·26, representing crystal content estimates in vol. % for dacite and andesite, respectively, and a critical crystallinity of 0·55, the viscosity of both magmas rises to $\sim 5 \times 10^3$ Pa s. However, if $\omega < 0{\cdot}55$, as suggested for Aleutian andesites, the 1835 andesite might have approached critical crystallinity, implying viscosities far exceeding those of crystal-poor magmas. It thus appears that the 1835 andesite, owing to its

much higher crystal content, was significantly more viscous than the silicic andesite and dacite magmas.

Plagioclase zoning, magnesium diffusion and associated timescales

Chemical zoning and diffusive equilibration in crystals can be used to estimate timescales of magmatic processes (e.g. Hawkesworth *et al.*, 2004; Costa & Morgan, 2010). This approach is well suited for plagioclase, which is widespread in igneous rocks and frequently zoned (Zellmer *et al.*, 1999; Costa *et al.*, 2003). Diffusion rates of various trace elements such as Li, Mg and Sr are several orders of magnitude faster than that of the anorthite component (e.g. Cherniak, 2010). Thus, whereas major elements record the conditions and processes that lead to plagioclase growth, trace elements can in addition provide information about the rates of these processes. Mg concentration in plagioclase is of particular interest because it can be used to track the degree of magmatic differentiation and can generally be measured using the electron microprobe (Costa *et al.*, 2003). However, modelling trace element diffusion in plagioclase is not straightforward owing to the effect of the chemical potential on partitioning and compositional dependence (Zellmer *et al.*, 1999; Costa *et al.*, 2003). We thus need to know how partitioning and diffusivity of trace elements is influenced by temperature and the major element composition (%An) of plagioclase (e.g. Bindeman *et al.*, 1998; Cherniak, 2010).

Plagioclase zoning patterns

Figure 10a shows the Mg content versus %An of plagioclase phenocrysts from the Cosigüina samples studied here. The Mg content of $An_{50–65}$ plagioclase varies between ~200 and 600 ppm (mean of ~380 ppm), without significant differences regardless of whether the crystals are hosted in dacite, silicic andesite or andesite. In addition, there is no obvious correlation between the Mg content and %An for $An_{50–65}$ plagioclase. In contrast, the Mg concentration in $An_{75–90}$ plagioclase is inversely correlated with the anorthite content. This relationship is especially marked for plagioclase in the pre-1835 basaltic andesite (Fig. 10a). The Mg content of plagioclase also varies according to host magma composition, with averages of 340 ppm in dacite, 400 ppm in silicic andesite, 440 ppm in andesite and 620 ppm in the basaltic andesite. A first-order interpretation of this variation is that the Mg content of $An_{75–90}$ plagioclase has been re-equilibrated via diffusion during residence in the andesite to dacite liquids. According to this scenario, the occasional plagioclase phenocrysts in the dacite that show an $An_{75–90}$ core overgrown by an $An_{50–65}$ rim probably record the most extreme re-equilibration of their core's Mg content to lower magmatic temperature conditions in a low-MgO liquid. This provides an opportunity to estimate their residence time in the dacite magma necessary for such diffusion to

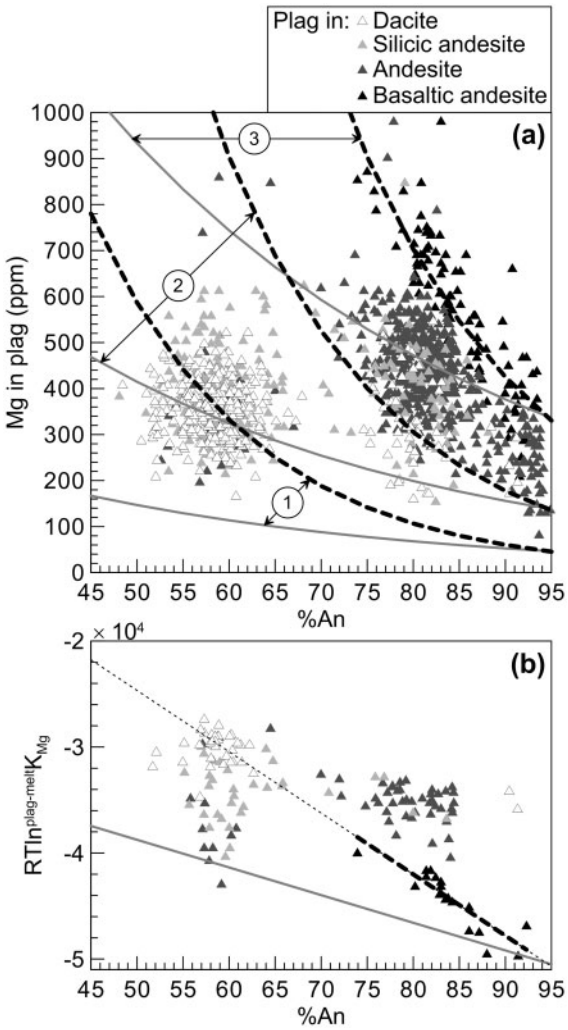

Fig. 10. Evidence for Mg diffusion in plagioclase and assessment of plagioclase–melt Mg partitioning. (a) Mg content vs %An of plagioclase in 1835 dacite (31 phenocrysts), silicic andesite (27 phenocrysts) and andesite (42 phenocrysts) and pre-1835 basaltic andesite (20 phenocrysts). Data from detailed traverses (Fig. 11) were excluded from this plot. It should be noted that $An_{75–90}$ plagioclase found in dacite, silicic andesite and andesite has a lower magnesium content than $An_{75–90}$ plagioclase found in basaltic andesite, suggesting that it has partly re-equilibrated with the silicic liquids. Continuous grey lines show Mg vs %An, calculated after Bindeman *et al.* (1998), for plagioclase equilibrated in liquids with (1) 1·1 wt % MgO (dacite glass) at 950°C, (2) 2·6 wt % MgO (andesite melt inclusion average) at 1010°C, and (3) 4·5 wt % MgO (basaltic andesite glass) at 1110°C. The equation of Bindeman *et al.* (1998) does not reproduce the observed Mg vs %An trends in Cosigüina plagioclase. Black dashed lines show the Mg vs %An of plagioclase calculated with a modified expression derived in (b). (b) Apparent plagioclase–melt Mg partition coefficients determined from Mg contents of phenocrysts rims and host matrix glass for the Cosigüina samples. Temperatures of 950, 960, 1010 and 1110°C were used for dacite, silicic andesite, andesite and basaltic andesite, respectively. The grey line corresponds to the Mg partitioning expression of Bindeman *et al.* (1998), which appears to underestimate $^{plag–liq}K_{Mg}$ values for Cosigüina plagioclase phenocrysts. The systematic increase in apparent $^{plag–liq}K_{Mg}$ values with decreasing %An for the pre-1835 basaltic andesite allows the formulation of a new expression for Mg partitioning for Cosigüina samples (bold dashed line and fine dashed extrapolation).

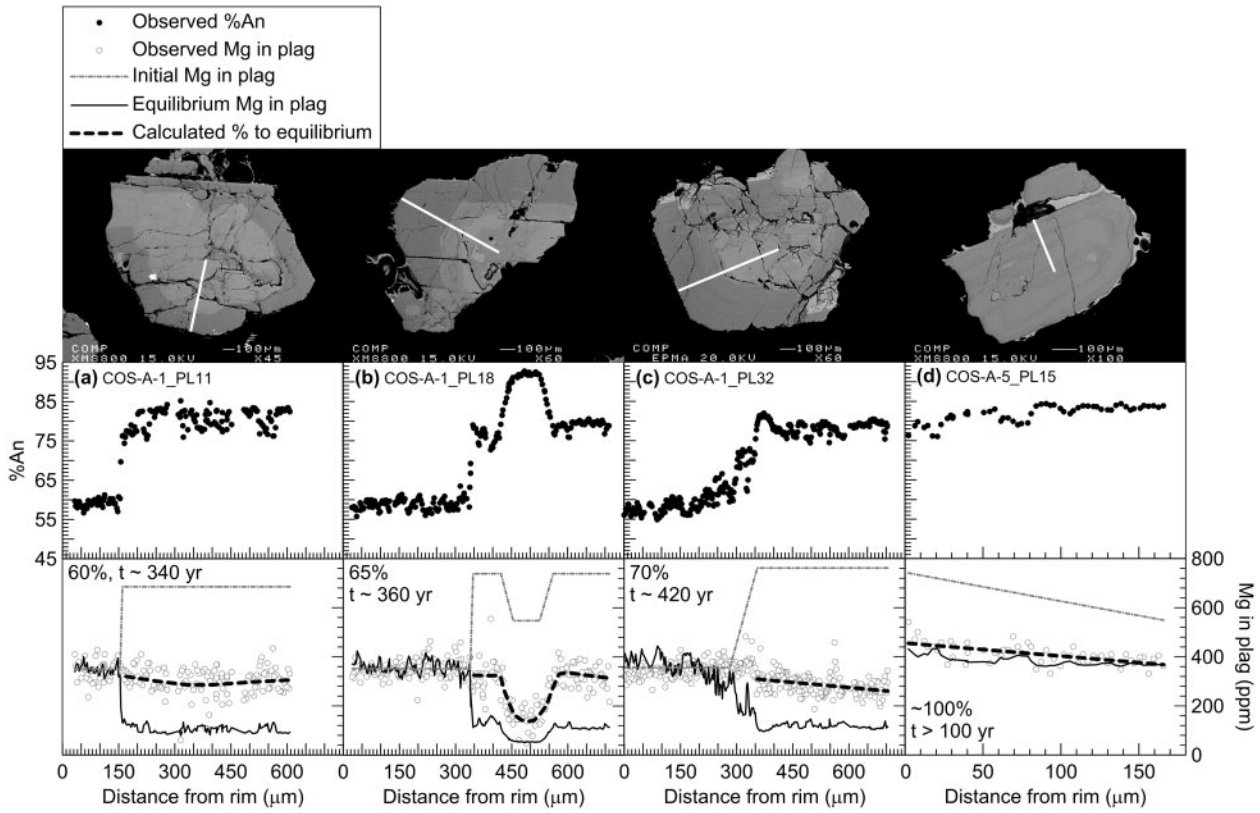

Fig. 11. Backscattered electron images, detailed electron microprobe traverses (anorthite and Mg contents), calculated initial and equilibrium Mg concentration, and degree of equilibration of Mg for selected plagioclase phenocrysts (see text for details). (a–c) Examples of phenocrysts found in dacite showing pronounced normal zoning, with an ~An_{80} core and ~An_{58} rim. The initial Mg concentration (grey dashed lines) of the calcic cores was calculated assuming crystallization from basaltic andesite and plagioclase–melt Mg partitioning governed by our modified equation (Fig. 10). Continuous black lines show the expected Mg concentration of the phenocrysts if fully equilibrated with dacite liquid. The extent of re-equilibration (% in upper left corners of bottom panels; bold dashed lines) of these phenocrysts is consistent with residence times in dacite of about 400 years. (d) Example of an An_{80} phenocryst found in andesite, showing modest normal zoning. The initial Mg concentration was calculated as for (a)–(c). In this case, the equilibrium Mg concentration was obtained assuming re-equilibration with andesite liquid. The observed Mg content of this phenocryst is consistent with nearly complete equilibration with andesite, requiring minimum residence time in this magma of about 100 years. (See main text and Fig. 12 for more details regarding the degree of equilibration and timescale determinations.)

take place (e.g. Costa *et al.*, 2003). We performed detailed core-to-rim electron microprobe traverses through selected plagioclase phenocrysts; four representative examples are shown in Fig. 11. Three of these crystals (Fig. 11a–c) are from the dacite and show an abrupt transition from a high-An core, ~500 μm to 1 mm in size, to a low-An rim, which is up to ~300 μm thick and has a mean Mg content of 350 ppm. The other phenocryst (Fig. 11d), hosted in andesite, displays modest normal core-to-rim zoning and slightly higher Mg. It should be noted that, in general, the Mg content of plagioclase tends to reflect a mirror image of the anorthite content.

Plagioclase–melt Mg partitioning

To derive timescale information from the observed Mg concentration in plagioclase, we need to estimate the Mg content of plagioclase at the time it crystallized (i.e. prior to diffusion), and to establish the boundary conditions under which diffusion took place [e.g. closed vs open boundary and constant vs changing boundary; see Costa *et al.* (2003) for details]. Partition coefficients for Mg between plagioclase and liquid ($^{plag-liq}K_{Mg}$) are thus required. Bindeman *et al.* (1998) derived the following relationship for plagioclase–basalt Mg partitioning:

$$RT\ln{}^{plag-liq}K_{Mg} = -26100X_{An} - 25700$$

where R is the ideal gas constant (8·3145 J mol^{-1} K^{-1}) and T is temperature in Kelvin. Using the above equation, we calculated the expected $^{plag-liq}K_{Mg}$ values and Mg contents of plagioclase equilibrated with dacite liquid (950°C, 1·1 wt % MgO), andesite liquid (1010°C, 2·6 wt % MgO) and basaltic andesite liquid (1110°C, 4·5 wt % MgO) (grey lines, Fig. 10a). We find that the equation of Bindeman *et al.* (1998) does not reproduce the observed steep Mg vs %An trends in Cosigüina $An_{75–90}$ plagioclase.

Figure 10b illustrates how apparent plagioclase–melt Mg partition coefficients for 1835 samples, for a given host liquid MgO content and temperature, exceed the values predicted by Bindeman *et al.* (1998). High apparent $^{plag-liq}K_{Mg}$ values have also been observed by other workers (see Bédard, 2006; Berlo *et al.*, 2007; Druitt *et al.*, 2012; J. Bédard, personal communication), particularly for low-An plagioclase and intermediate to silicic liquid compositions. This suggests that the relationship of Bindeman *et al.* (1998), which was derived for basaltic bulk compositions, probably underestimates $^{plag-liq}K_{Mg}$ in certain cases. The alternative would imply that all crystals studied here are in disequilibrium with their host melt in terms of Mg, which seems highly unlikely, particularly considering the rapid diffusivity of Mg in plagioclase. We thus developed a new expression based on our samples and observations. Apparent $^{plag-liq}K_{Mg}$ values in pre-1835 basaltic andesite (determined from the Mg contents of plagioclase rims and host matrix glass) increase linearly with decreasing %An and are unlikely to have been affected by diffusion. They were thus chosen for the regression, yielding the following expression (Fig. 10b, bold dashed line):

$$RT^{plag-melt}K_{Mg} = -57800X_{An} + 4300.$$

This equation has an R^2 of 0·77 for the basaltic andesite data and, when extrapolated to low anorthite content, also captures the apparent $^{plag-liq}K_{Mg}$ values obtained for 1835 dacite–plagioclase rim pairs (Fig. 10b, fine dashed line). We thus use this expression, which is valid only for the composition and temperature ranges of our study, for the diffusion modelling presented below.

Diffusion modelling approach and results

Here we are mainly interested in the re-equilibration of the calcic, $An_{75–90}$ portions of the phenocrysts, which appear to have grown largely from basaltic andesite although some may have formed from mafic, undegassed andesite (Figs 9c and 10) (see Discussion). The initial Mg concentration in $An_{75–90}$ plagioclase was thus calculated assuming crystallization from a liquid with 4·5 wt % MgO and a temperature of 1110°C (Fig. 11). For $An_{50–65}$ plagioclase, we used a liquid with 1·1 wt % MgO at 950°C. We used a constant composition and open flux condition at the boundary, meaning that re-equilibration was assumed to have occurred only once and with a liquid of the host glass composition. We used the diffusion coefficient of Van Orman *et al.* (2014) for anorthite. With these conditions, we can calculate the degree of equilibration of each phenocryst, which is found to range from ~50 to 100% (see Figs 11 and 12 for details). Phenocrysts that are fully re-equilibrated yield timescale minima.

The determination of timescales from diffusion models gives robust results when detailed concentration profiles

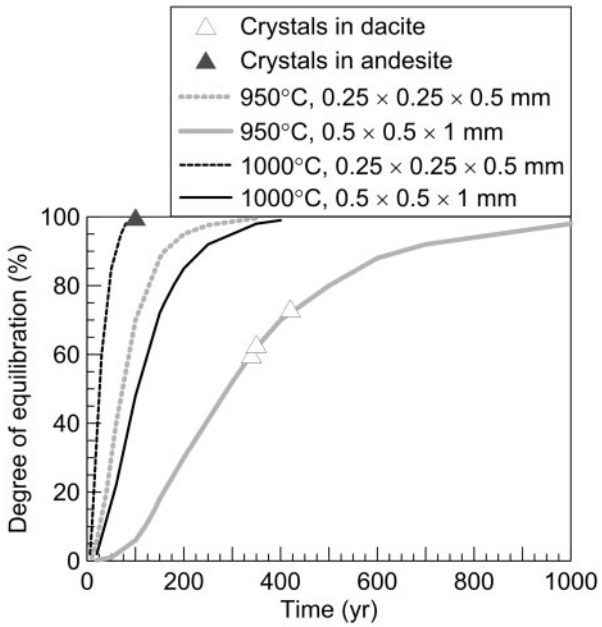

Fig. 12. Model of the degree of equilibration of Mg in plagioclase as a function of time. Equilibration % = 100 − 100 × [($^{measured}C_{Mg}$ − $^{equilibrium}C_{Mg}$)/($^{initial}C_{Mg}$ − $^{equilibrium}C_{Mg}$)]. Curves show diffusion calculations for the equilibration of the Mg concentration at the centre of an An_{85} plagioclase crystal using the 3D analytical solution for a parallelepiped (Crank, 1975) of two different sizes (0·5 × 0·5 × 1 and 0·25 × 0·25 × 0·5 mm) and at two temperatures (950 and 1000°C), reflecting reasonable conditions for the Cosigüina samples. Calculated degrees of equilibration and diffusion times for the natural phenocrysts shown in Fig. 11 are also plotted.

can be fitted (e.g. Druitt *et al.*, 2012). Unfortunately, this approach cannot be used for the Cosigüina samples, in part owing to the significant scatter of the Mg data, but mainly because the extent of re-equilibration is very large. In such a situation, the effects of diffusion in multiple dimensions become important, and a realistic fit of the profiles would require the use of a detailed 3D model that considers the crystal shape. Moreover, because many 1835 plagioclase phenocrysts are broken, it is not always possible to precisely determine their actual sizes. Given these limitations of the data, we have opted to develop a first-order model of the Mg concentration in the phenocryst cores using an analytical solution of the diffusion equation for a parallelepiped (Crank, 1975) and approximate phenocryst sizes assuming that the third dimension is twice the longest one seen in two dimensions, as suggested by our petrographic observations. We then calculated the time necessary for the degree of equilibration at the centre of the modelled crystals to match that obtained for the natural phenocrysts. We find that the three $An_{75–90}$ cores shown in Fig. 11a–c probably equilibrated with the dacite host for ~400 years (Fig. 12). In addition, $An_{75–90}$ phenocrysts from the andesite appear to be almost completely re-equilibrated, requiring minimum residence times of ~100 years in the andesite (Figs 11d and 12). Our approach

probably yields a first-order time estimate, except when the degree of re-equilibration nears 100%, but a rigorous quantification of the uncertainties involved is difficult. However, the main parameters controlling the re-equilibration times, such as the relatively large sizes of the crystals (>500 μm), the temperature (>930°C) and the large degree of equilibration (>50%), are well constrained. With these constraints, the model results imply that the timescales we report cannot be longer than a factor of five; that is, residence times probably did not exceed ~2000 years.

DISCUSSION

We now develop a petrogenetic model based on the results presented above. We first focus on the origin of the 1835 andesite and on the development of magma reservoir stratification. Then we discuss the implications of Mg diffusion in plagioclase for timescales of magma differentiation at Cosigüina. After addressing potential eruption triggers and catastrophic syn-eruptive degassing, we touch briefly on possible future eruption scenarios at Cosigüina and end with a comparison with similar compositionally zoned systems.

Petrogenetic model

Parental magmas and origin of the andesite

The 1835 andesite is characterized by bimodal to trimodal crystal populations, dominated by abundant $An_{75–90}$ plagioclase (Figs 7c and 8). The $An_{75–90}$ phenocrysts, in contrast to $An_{50–65}$ plagioclase, are commonly sieve-textured and contain numerous melt inclusions and channels of andesitic composition (Fig. 3h and i). Although plagioglase–melt hygrometry shows that such calcic plagioclase may crystallize from hydrous andesite at 1010°C (Fig. 9c), as opposed to what might be expected from MELTS simulations (Supplementary Data Fig. A2) (see also Panjasawatwong *et al.*, 1995), their Mg content still appears too high to be in equilibrium with andesite (Fig. 10). Instead, many of these crystals probably formed from more mafic liquids, consistent with the composition of plagioclase ($An_{75–95}$) found in the pre-1835 basaltic andesite (Fig. 7d). The occurrence of magnesian clinopyroxene inclusions within the calcic plagioclase phenocrysts supports this interpretation. Based on the above, magma mixing between a resident dacite and an invading basaltic andesite may initially appeal as an attractive mechanism to produce the 1835 andesite and trigger the eruption. A strong case for such a situation has been demonstrated at several andesitic subduction zone volcanoes (e.g. Anderson, 1976; Murphy *et al.*, 1998; Clynne, 1999; Costa & Singer, 2002; Ruprecht *et al.*, 2012). However, multiple lines of evidence argue against a magma mixing origin for the Cosigüina andesite. (1) In bivariate diagrams the major and trace element composition of the andesite is not collinear with that of the pre-1835 basaltic andesite and 1835 dacite (Figs 5c, e and 6a). (2) The andesite bulk-rock trend requires a component of accumulated plagioclase (see below). (3) The andesite lacks olivine, which is common in the basaltic andesite, and also lacks both macroscopic and microscopic magma mingling textures (e.g. banded pumice or scoria and mafic magma enclaves).

In Fig. 5, andesite bulk-rocks, as well as that of the pre-1835 basaltic andesite, plot off the Al_2O_3 and FeO* trends defined by matrix glasses, melt inclusions and silicic andesite and dacite bulk-rocks, a feature that is also observed in older Cosigüina tephras (M.-A. Longpré, unpublished data). This departure from Cosigüina's liquid line of descent, to higher Al_2O_3 and lower FeO* at given SiO_2, indicates that the andesite bulk-rocks do not represent purely melt compositions, but rather mixtures of silicic andesite liquid and accumulated crystals, largely plagioclase. Mass-balance calculations reproduce the andesite bulk-rock trend by addition of 15–33 wt % plagioclase ($An_{75–90}$), 2–4 wt % clinopyroxene, up to 3 wt % orthopyroxene and up to 2 wt % magnetite to the silicic andesite bulk-rock composition (Table 4). Despite this partly cumulate origin, both the andesite and basaltic andesite bulk-rocks retain a negative Eu anomaly (Fig. 6d), implying that the liquid fraction had undergone extensive plagioclase removal in an earlier stage of differentiation. We thus propose that a significant portion of the crystal cargo, particularly the $An_{75–90}$ plagioclase, observed in the andesite is residual from differentiation of parental basalt and basaltic andesite magmas, probably taking place in the lower crust (Fig. 13) (e.g. Annen *et al.*, 2006). As these low-viscosity mafic magmas rose to the upper crust, decompression under H_2O-undersaturated conditions caused partial dissolution of plagioclase phenocrysts and infiltration of andesitic liquids (Nelson & Montana, 1992). Upon intersection of the H_2O-saturated liquidus, degassing-induced crystallization sealed the inclusions and channels inside the crystals, creating the sieve texture (e.g. Berlo *et al.*, 2007).

Magma reservoir zonation

The 1835 eruptive sequence, starting with small volumes of crystal-poor dacite pumice and silicic andesite scoria followed after an apparent lull of ~12 h by ~3 km^3 (bulk) of crystal-rich andesite scoria, suggests tapping of a stratified, albeit dominantly andesitic magma reservoir. The chemical and mineralogical affinities and thermal continuity of the 1835 magmas provide evidence that the dacite and silicic andesite were derived from the andesite magma through upward segregation of silicic andesite liquid (glass composition of the andesite) followed by fractional crystallization. For example, silicic andesite and dacite bulk-rocks, matrix glasses and melt inclusions fall on the liquid line of descent of the Cosigüina magmas, together with andesite glass and melt inclusions

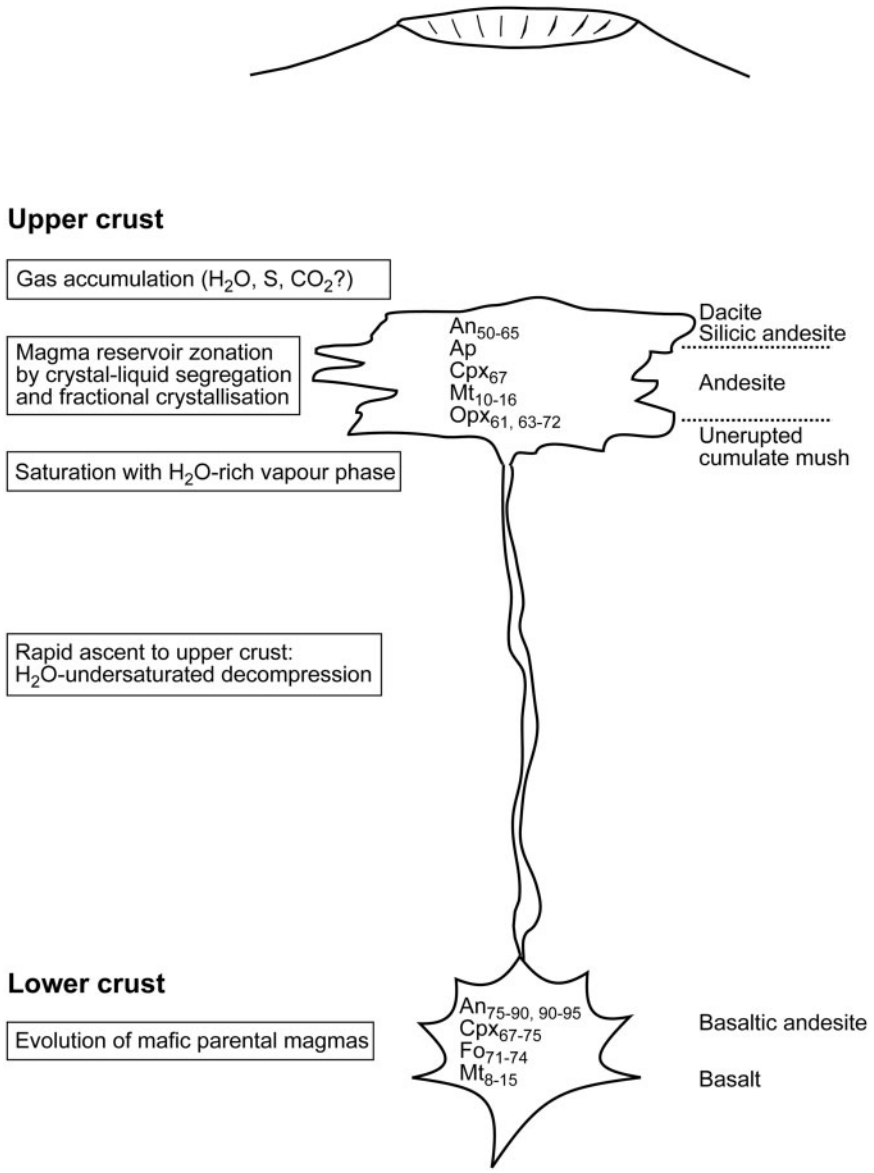

Fig. 13. Conceptual model of the magma plumbing system beneath Cosigüina. In the lower crust, H_2O-undersaturated basaltic to basaltic andesite magmas evolved and crystallized mafic phenocrysts (olivine, $An_{75–90}$ plag, high-Al_2O_3 $Cpx_{67–75}$, ± magnetite). Upon rapid ascent to the upper crust, H_2O-undersaturated decompression caused resorption (formation of sieve texture) of calcic plagioclase. The ascending magma, now of basaltic andesite to andesite composition, reached saturation with an H_2O-rich vapour phase and intersected its H_2O-saturated liquidus as it stalled in a shallow magma reservoir. Degassing and crystallization increased magma viscosity. Melt inclusions and channels formed during decompression were sealed in calcic plagioclase. Hindered settling, compaction and gas-driven filter pressing caused the segregation of crystal-poor, partly degassed silicic andesite liquid, which rose to the upper part of the magma reservoir. The andesite to silicic andesite liquid, now volatile-saturated at lower pressure and temperature conditions, crystallized a new mineral assemblage consisting of $An_{50–65}$ plagioclase, Cpx_{67}, $Opx_{63–72}$ and magnetite. Fractional crystallization of this assemblage drove the melt composition towards dacite in the upper part of the reservoir. When dacitic compositions were reached, Opx_{61} and apatite began crystallizing. Heat supplied from the underlying andesite body kept the silicic andesite and dacite magmas crystal-poor. Gradual accumulation of a free gas phase, rich in H_2O, S and CO_2(?) in the apical part of the magma reservoir, led to pressure buildup, eventually triggering the 1835 eruption.

(Fig. 5). In addition, depletion of compatible elements such as Sr and V and enrichment of incompatible elements such as K, Rb, Zr and Ba from andesite to dacite bulk-rocks are consistent with this crystal–liquid segregation and fractional crystallization scenario. Systematic increase in REE concentrations and parallel REE patterns characterized by increasingly negative Eu anomalies from basaltic andesite to dacite (Fig. 6) further support this interpretation, and no extraneous contribution (i.e. assimilation of crustal rocks) to the dacite is chemically

identifiable. Based on mass balance, the dacite liquid can be produced from the silicic andesite liquid through fractional crystallization of ~12 wt % plagioclase, 3 wt % orthopyroxene, 2 wt % magnetite, 2 wt % clinopyroxene, and <1 wt % apatite (Fig. 5, Table 4). The presence of euhedral, weakly zoned $An_{50–65}$ plagioclase throughout the 1835 deposits, although in minor proportions in andesite, implies crystallization of this phase starting with andesitic liquid (Fig. 7), in agreement with MELTS models (Supplementary Data Fig. A2). Thus, the occurrence of $An_{50–65}$ plagioclase as a component of polyphase glomerocrysts is consistent with a multiply saturated andesite liquid evolving towards dacitic compositions. Finally, our thermometry results indicate thermal continuity from 930–950°C for dacite to 960–1010°C for silicic andesite and the main andesite body, suggesting that the magmas were physically contiguous. The large reservoir of hot, crystal-rich andesite thus served both as the source of the extracted liquid and as a proximate heat source to maintain the crystal-poor nature of the overlying silicic andesite and dacite (e.g. Hildreth & Fierstein, 2000).

We propose that the following sequence of events occurred within Cosigüina's shallow crustal magma reservoir leading to the 1835 eruption (Fig. 13). Periodic influx of crystal-rich basaltic andesite to andesite magmas from depth provided new material and heat to the bottom of the shallow reservoir. Owing to decompression, the magma feeding the shallow reservoir became saturated with an H_2O-rich vapour phase. Rapid and vigorous degassing lowered H_2O and other volatiles in the mafic andesite liquid, increased its viscosity, and drove crystallization and differentiation towards silicic andesite. At this point, the magma reached a high crystallinity, favouring crystal–liquid separation by hindered settling, compaction and gas-driven filter pressing (e.g. Sisson & Bacon, 1999; Bachmann & Bergantz, 2004; Dufek & Bachmann, 2010; Deering *et al.*, 2011). Progressive roofward escape of gas bubbles and silicic andesite liquid produced a thin, crystal-poor layer of bubbly magma in the apical region of the reservoir. Now suddenly partly degassed and at lower temperature, this more evolved liquid began crystallizing a distinct mineral assemblage including $An_{50–65}$ plagioclase. Further fractional crystallization of this new mineral assemblage produced dacite liquid, which segregated to the top of the reservoir owing to its lower density. The liquid extraction process yielded a crystal mush in the lower part of the magma reservoir. The 1835 andesite probably contains crystals accumulated in this manner, but its moderate crystallinity (Table 4) indicates that a deeper crystal-rich residue was not erupted in 1835 (Fig. 13).

Timescales of magmatic differentiation

Constraints on timescales of magmatic differentiation through fractional crystallization largely come from U-series disequilibria studies (Hawkesworth *et al.*, 2000). Several studies indicate magma evolution over comparatively long timescales (10^4–10^5 years) (Hawkesworth *et al.*, 2000, and references therein), but examples also exist for which magma differentiation and reservoir zonation through fractional crystallization were inferred to occur within 10^2–10^3 years (Widom *et al.*, 1992; Bourdon *et al.*, 1994; Condomines *et al.*, 1995; Rogers *et al.*, 2004). Bachmann & Bergantz (2004) calculated that segregation through hindered settling of large volumes (>500 km^3) of viscous (10^5 Pa s), crystal-poor rhyolite from a silicic mush requires 10^4–10^5 years for small crystal sizes (1–2 mm). With magma volumes and viscosities two orders of magnitude smaller at Cosigüina, shorter timescales may be expected for the crystal–liquid separation process. Residence times of ~400 years, with a maximum of the order of 2000 years, for $An_{75–90}$ plagioclase cores in dacite may record a significant mafic magma influx to the reservoir a few hundred years before 1835. As the differentiation process probably had already been continuing when the crystals were entrained in the silicic magma, the timescales that we calculate probably pertain to only a fraction of the total period of chemical evolution of the magma. Nevertheless, we speculate that magmatic differentiation from basaltic andesite to dacite and development of chemical zonation in the shallow magma reservoir occurred rapidly at Cosigüina, on timescales of 10^2–10^3 years. This is consistent with stratigraphic evidence; the pre-1835 mafic tephras at locality 3, including the basaltic andesite studied here, occur within a thick sequence of paleosols above an older zoned plinian fall deposit, indicating mafic magma replenishment of the system possibly 10^2–10^3 years prior to 1835 (see Scott *et al.*, 2006).

If the stratigraphic sequence at locality 3, comprising the deposits of >15 compositionally zoned eruptions, is of comparable age to the oldest dated lavas of the neighbouring San Cristóbal and Telica volcanoes (160–330 ka, Carr *et al.*, 2007), a maximum recurrence time for repeated replenishment, magma reservoir zonation and eruption at Cosigüina is ~$(1–2) \times 10^4$ years. Detailed geochronology will allow us to better constrain the timescales of magma reservoir zonation at Cosigüina.

Eruption triggers

Of particular interest from a volcanological perspective are the triggering mechanisms of large explosive eruptions. In some cases, eruptions may be triggered by earthquakes (e.g. Manga & Brodsky, 2006). 'Shocks' and earthquakes in the vicinity of Cosigüina mentioned in historical reports correspond to syn-eruptive seismicity (Galindo, 1835*a*, 1835*b*; Caldcleugh, 1836) and were thus probably of volcano-tectonic origin. A search using the Significant Earthquake Database (National Geophysical Data Center/World Data Service (NGDC/WDS) Significant Earthquake Database, Boulder, CO, USA, available at http://www.ngdc.noaa.gov/nndc/struts/form?t=101650&s=

l&d=l) returned no result within ~1000 km of the volcano in the decade preceding the eruption. The M8·5 1835 Chile earthquake occurred on 20 February (Darwin, 1840), a month after the eruption, and thus cannot be considered a candidate. We would expect a significant regional earthquake (e.g. >M6) prior to 20 January 1835 to appear in the historical record; there is therefore no direct evidence of an external seismic trigger.

Renewed injections of hot, mafic magma into a silicic magma reservoir are commonly inferred to destabilize the system, resulting in an eruption (Sparks *et al.*, 1977). As we state above, however, the 1835 andesite is unlikely to be the hybrid product of an influx of fresh mafic magma in a dacitic magma reservoir immediately preceding the eruption. There is stratigraphic evidence for mafic magma replenishment 10^2–10^3 years prior to 1835, and we have shown that the pre-1835 basaltic andesite was probably parental to the 1835 magmas. Some of this mafic material may have continued to feed the lower part of the magmatic system periodically prior to eruption, supplying heat and calcic plagioclase phenocrysts to the overlying andesite. Thus, although the evidence is scarce, we cannot rule out the possibility that fresh mafic magma entering the system provided the eruption trigger, but was not erupted.

Another commonly invoked eruption trigger mechanism for intermediate to silicic systems is the oversaturation of magma with respect to volatile species, the exsolution of which gradually causes an increase in magmatic pressure until fracturing of the magma reservoir roof results in an eruption (e.g. Blake, 1984; Tait *et al.*, 1989). We have demonstrated that the 1835 magmas were saturated with an H_2O-rich vapour phase, implying a significant amount of volatile exsolution within the shallow magmatic system during chemical evolution. We propose that, after initial H_2O saturation (first boiling), the Cosigüina magmas underwent continued exsolution of gas bubbles driven by crystallization (second boiling), leading to the accumulation of a volumetrically important gas phase at the apex of the magma reservoir over time. Coupled with periodic influx of fresh, volatile-rich magma into the bottom of the reservoir and magma buoyancy (Caricchi *et al.*, 2014; Malfait *et al.*, 2014), this is likely to have led to critical overpressurization of the system, triggering the eruption.

Magma degassing and sulphur yield to the atmosphere

Catastrophic release of this exsolved gas phase is likely to have occurred at the eruption onset, contributing to rapid ejection of dacite and silicic andesite magmas. Volatile species that were in solution also largely escaped from the magma at this point, as documented through substantial loss of H_2O, S and, to a lesser extent, Cl from 1835 melt inclusions to matrix glasses (Fig. 4). This may have induced rapid microlite growth in the andesite magma (Fig. 3g). In turn, the degassing may have amplified the viscosity contrast between crystal-poor, bubble-rich dacite and silicic andesite and crystal-rich andesite, creating a rheological boundary that may have delayed the course of the eruption (i.e. the hiatus between phase 1 and phase 2) (e.g. Stix & Kobayashi, 2008).

The evidence presented here for significant sulphur degassing associated with the 1835 event contrasts strongly with the results of Palais & Sigurdsson (1989) that suggested little sulphur release. Our results require a reassessment of the eruption's sulphur yield to the atmosphere and its climatic impact (see Self *et al.*, 1989). In a companion study (Longpré *et al.*, in preparation) we consider the contributions of the exsolved gas phase present in the reservoir prior to eruption as well as syn-eruptive devolatilization of the melt, using the 'petrologic method' (Devine *et al.*, 1984; Palais & Sigurdsson, 1989; Scaillet *et al.*, 2003), to estimate the sulphur yield of the eruption. Our results, coupled with ice core data acquired since the late 1980s (e.g. Gao *et al.*, 2008), provide strong evidence that the Cosigüina eruption was one of the most important sulphur-producing events of the last few hundred years. The atmospheric impact of the eruption was sizeable and comparable with or even larger than that of the 1991 eruption of Pinatubo (e.g. Robock, 2002). This is supported by temperature-sensitive tree-ring chronologies (e.g. Briffa *et al.*, 1998), suggesting Northern Hemisphere cooling in 1835, 1836 and 1837 in response to the eruption.

Prehistoric and future Cosigüina eruptions

Little work has been done so far on prehistoric volcanism at Cosigüina. Hradecký *et al.* (2001) and Hradecký & Rapprich (2008) used mapping, ^{14}C ages and correlations of pyroclastic units to divide the activity of the volcano into five sequences, all of which were interpreted to be younger than ~500 BP. Near-continuous outcrops at locality 3 (Fig. 1) expose ~75 m of stratigraphy, revealing pyroclastic fall and flow deposits of tens of pre-1835 eruptions [see also locality H of Scott *et al.* (2006)]. As pointed out by Scott *et al.* (2006), many of these pyroclastic fall deposits are thicker and coarser than the 1835 ash and scoria, which cap the sequence and occur above a thick succession of brown to orange paleosols. The thick paleosols, coupled with the lack of historical records for multiple, large explosive eruptions at Cosigüina prior to 1835 (see list of unconfirmed pre-1835 eruptions: Siebert & Simkin, 2002; Scott *et al.*, 2006), imply that this sequence must be several thousands of years old (Scott *et al.*, 2006), rather than historical in age (Hradecký & Rapprich, 2008). The character of the prehistoric deposits exposed at locality 3 indicates that Cosigüina has produced >15 compositionally zoned explosive eruptions in the past, with as yet unknown frequency. In case of reawakening, future eruption scenarios on the scale of the 1835 event or larger should be envisaged (Scott *et al.*, 2006). Detailed stratigraphic,

geochronological and geochemical work on the sequence at locality 3 is in progress.

Comparison with other compositionally zoned systems

The products of the 1835 Cosigüina eruption share many similarities with well-known compositionally zoned pyroclastic deposits, such as those of the climactic eruption of Mount Mazama (Bacon, 1983; Bacon & Druitt, 1988), the 1912 eruption at Novarupta–Katmai (e.g. Hildreth, 1983; Hildreth & Fierstein, 2000), the AD 79 'Pompei' eruption of Vesuvius (Civetta *et al.*, 1991*l*; Cioni *et al.*, 1995; Landi *et al.*, 1999) and the 1883 eruption of Krakatau (Mandeville *et al.*, 1996). We now briefly compare these with Cosigüina.

The ~7000 BP eruption of Mount Mazama ejected ~50 km^3 dense rock equivalent (DRE) of magma to form the Crater Lake caldera (Bacon, 1983). In this event, moderately porphyritic rhyodacite, representing most of the ejecta, was erupted first, followed by subordinate crystal-rich andesite and mafic andesite. The compositional and thermal (Fe–Ti oxide thermometry) data led Bacon (1983) and Bacon & Druitt (1988) to develop a magma reservoir model in which the rhyodacite was produced by fractional crystallization of andesite liquid, accumulating in the upper part of the reservoir by upward escape of buoyant liquid. Similar to Cosigüina and Katmai, the mafic end-member magma at Mazama is markedly richer in phenocrysts than the silicic end-member. Interestingly, Mazama plagioclase analyses reported by Druitt & Bacon (1989) show two distinct populations in terms of anorthite content, namely $An_{25–60}$ and $An_{75–90}$, with only a few analyses falling in the $An_{60–75}$ range, a situation analogous to that of Cosigüina. Those workers considered the low-An population to have formed from andesite to rhyodacite liquids, whereas the calcic plagioclase was thought to originate from mafic liquids. As regards volatile elements, Mandeville *et al.* (2009) showed that the Mazama magma was saturated with a vapour phase and that substantial amounts of H_2O, S and Cl had exsolved from the melt prior to eruption. Differences between Mazama and Cosigüina include (1) the much greater volume of erupted magma, (2) the occurrence of two distinct magma types (low- and high-Sr liquids) and (3) the much higher proportion of silicic magma at Mazama.

The ejecta of the 1912 eruption at Novarupta–Katmai is another classic example of a compositionally zoned pyroclastic deposit (Hildreth, 1983). The world's largest 20th century eruption produced 7–8 km^3 of near-aphyric high-silica rhyolite, followed by 4·5 km^3 of crystal-rich dacite and 1 km^3 of crystal-rich andesite (all DRE values) (Hildreth & Fierstein, 2000). Extensive chemical and isotopic data coupled with Fe–Ti oxide temperature and fO_2 estimates demonstrate that the rhyolite originated mainly from progressive roofward segregation of interstitial liquid from an underlying zoned body of mushy dacite to andesite (Hildreth & Fierstein, 2000). Differences from Cosigüina include a much wider compositional range and a higher proportion of the silicic end-member magma at Novarupta–Katmai; similarities include the crystal-poor nature of the silicic magma and its saturation with respect to volatile species (Lowenstern, 1993). We note that sieve-textured plagioclase is rare in the 1912 rhyolite and dacite but abundant in the andesite scoria. Feldspars with calcic compositions (up to An_{94}) are also found in Novarupta–Katmai andesite (Hildreth, 1983; Hildreth & Fierstein, 2012).

With its size, morphology (e.g. its prominent somma rim) and recurrent compositionally zoned explosive eruptions, Cosigüina shows striking resemblance to Mount Vesuvius. Several plinian deposits of Vesuvius, including that of the famous AD 79 'Pompei' eruption, are compositionally zoned and best explained as derived from a stratified magma reservoir (Civetta *et al.*, 1991*l*; Landi *et al.*, 1999). In AD 79, about 1–1·5 km^3 of magma (DRE) was erupted; 25–30% as white phonolite pumice and 70–75% as grey tephriphonolite pumice (Cioni *et al.*, 1995, 1999). Cioni *et al.* (1995) argued that the phonolite was derived from the upper, cooler part of the shallow magma reservoir and evolved largely through crystal fractionation. Those researchers proposed that grey tephriphonolite pumice originated from syn-eruptive mixing of a superheated crystal-poor phonotephrite magma stored in the lower part of the reservoir with overlying phonolite magma and incorporation of cumulate crystals from the magma reservoir walls. Although CO_2 and S degassing occurred in the AD 79 reservoir, it appears that saturation with an H_2O-rich vapour phase occurred only upon eruption (Cioni, 2000). Thus, although some of the processes invoked to explain the compositional grading at Vesuvius are analogous to those described in the present study, the two cases also show important differences in magma composition, mineralogy and the development of reservoir stratification.

CONCLUSIONS

The main conclusions of this work may be summarized as follows.

(1) The 1835 eruption of Cosigüina volcano was fed by a compositionally and thermally zoned magma reservoir. Small volumes of dacite and silicic andesite were erupted first, followed by andesite in the second and major phase of the eruption. Magma reservoir zonation was brought about by incremental separation of crystal-poor silicic andesite liquid from the main crystal-rich magma body, through hindered settling, compaction and gas-driven filter pressing. Fractional crystallization of this crystal-poor magma produced

buoyant dacite liquid, which accumulated at the top of the magma reservoir.

(2) The andesite contains abundant calcic plagioclase phenocrysts, largely inherited from earlier stages of differentiation of mafic parental magmas in the lower crust. The andesite bulk-rocks do not represent liquid compositions, but rather mixtures of andesite liquid and an accumulated mineral assemblage composed mostly of plagioclase.

(3) The calcic plagioclase phenocrysts in the 1835 magmas show evidence for extensive re-equilibration of their Mg content via diffusion. Modelling of the diffusion process constrains the residence time of these crystals in the intermediate to silicic magmas to more than 100 years and less than ~2000 years, with detailed study of three crystals yielding ~400 years. Although these crystal residence times represent minimum magma differentiation times, we propose that the development of chemical zonation in stratovolcano magma reservoirs may occur over such relatively short timescales.

(4) There is limited evidence for mafic magma influx shortly before the 1835 eruption. Gradual accumulation of a free gas phase near the apex of the Cosigüina magma reservoir, first through initial H_2O saturation and then driven by progressive crystallization, appears to be a viable mechanism to trigger the eruption.

(5) Our results, coupled with ice core data acquired since the late 1980s, suggest that the 1835 Cosigüina eruption was one of the most important sulphur-producing events of the past few centuries. The atmospheric impact of the eruption was substantial and comparable with that of the 1991 Pinatubo eruption.

(6) Prehistoric pyroclastic deposits at Cosigüina are typically thicker and coarser than the 1835 deposit at a particularly well-exposed stratigraphic section located 11 km west of the caldera, demonstrating that Cosigüina has produced recurrent large explosive eruptions in the past. In case of future unrest, eruption scenarios on the scale of the 1835 event or larger should be envisaged.

ACKNOWLEDGEMENTS

We thank INETER personnel for their help in organizing field logistics, and Erika Anderson, Jack Wilcock and Gregor Lucic for assistance with fieldwork. We are indebted to Mike Vogelsang and Stacy Sabo-Vogelsang for their hospitality at Redwood Beach Resort in Mechapa during fieldwork. Lang Shi provided invaluable support and advice for microprobe analyses, and Glenna Keating and William Minarik conducted the XRF and ICP-MS work. Discussions with Don Baker and Jason Coumans, reviews by Georg Zellmer, Olivier Bachmann and Steffen Kutterolf, and editorial handling by Simon Turner helped improve this paper. We also thank Thor Hansteen and Cosima Burkert for pointing out the occurrence of fluid inclusions in the 1835 samples and sharing their pictures.

FUNDING

This research was funded through R. H. Tomlinson, Fonds de recherche du Québec–Nature et technologies (FRQNT), and Natural Sciences and Engineering Research Council of Canada (NSERC) postdoctoral fellowships to M.-A.L. and NSERC Discovery and Accelerator grants to J.S.

SUPPLEMENTARY DATA

Supplementary data for this paper are available at *Journal of Petrology* online.

REFERENCES

Andersen, D. J., Lindsley, D. H. & Davidson, P. M. (1993). QUILF: A Pascal program to assess equilibria among Fe–Mg–Mn–Ti oxides, pyroxenes, olivine, and quartz. *Computers and Geosciences* **19**, 1333–1350.

Anderson, A. T. (1976). Magma mixing: petrological process and volcanological tool. *Journal of Volcanology and Geothermal Research* **1**, 3–33.

Angell, J. K. & Korshover, J. (1985). Surface temperature changes following the six major volcanic episodes between 1780 and 1980. *Journal of Climate and Applied Meteorology* **24**, 937–951.

Annen, C., Blundy, J. D. & Sparks, R. S. J. (2006). The genesis of intermediate and silicic magmas in deep crustal hot zones. *Journal of Petrology* **47**, 505–539.

Bachmann, O. & Bergantz, G. W. (2004). On the origin of crystal-poor rhyolites: extracted from batholithic crystal mushes. *Journal of Petrology* **45**, 1565–1582.

Bacon, C. R. (1983). Eruptive history of Mount Mazama and Crater Lake Caldera, Cascade Range, U.S.A. *Journal of Volcanology and Geothermal Research* **18**, 57–115.

Bacon, C. R. & Druitt, T. H. (1988). Compositional evolution of the zoned calcalkaline magma chamber of Mount Mazama, Crater Lake, Oregon. *Contributions to Mineralogy and Petrology* **98**, 224–256.

Barclay, J., Rutherford, M. J., Carroll, M. R., Murphy, M. D., Devine, J. D., Gardner, J. & Sparks, R. S. J. (1998). Experimental phase equilibria constraints on pre-eruptive storage conditions of the Soufrière Hills magma. *Geophysical Research Letters* **25**, 3437–3440.

Bédard, J. H. (2006). Trace element partitioning in plagioclase feldspar. *Geochimica et Cosmochimica Acta* **70**, 3717–3742.

Berlo, K., Blundy, J., Turner, S. & Hawkesworth, C. (2007). Textural and chemical variation in plagioclase phenocrysts from the 1980 eruptions of Mount St. Helens, USA. *Contributions to Mineralogy and Petrology* **154**, 291–308.

Bindeman, I. N., Davis, A. M. & Drake, M. J. (1998). Ion microprobe study of plagioclase–basalt partition experiments at natural concentration levels of trace elements. *Geochimica et Cosmochimica Acta* **62**, 1175–1193.

Blake, S. (1984). Volatile oversaturation during the evolution of silicic magma chambers as an eruption trigger. *Journal of Geophysical Research* **89**, 8237–8244.

Blundy, J. & Cashman, K. (2008). Petrologic reconstruction of magmatic system variables and processes. In: Putirka, K. D. & Tepley, F. J., III (eds) *Minerals, Inclusions and Volcanic Processes. Mineralogical Society of America and Geochemical Society, Reviews in Mineralogy and Geochemistry* **69**, 179–239.

Bourdon, B., Zindler, A. & Wörner, G. (1994). Evolution of the Laacher See magma chamber: Evidence from SIMS and TIMS measurements of U–Th disequilibria in minerals and glasses. *Earth and Planetary Science Letters* **126**, 75–90.

Boynton, W. V. (1984). Geochemistry of the rare earth elements: meteorite studies. In: Henderson, P. (ed.) *Rare Earth Element Geochemistry*. Amsterdam: Elsevier, pp. 63–114.

Briffa, K. R., Jones, P. D., Schweingruber, F. H. & Osborn, T. J. (1998). Influence of volcanic eruptions on Northern Hemisphere summer temperature over the past 600 years. *Nature* **393**, 450–455.

Caldcleugh, A. (1836). Some account of the volcanic eruption of Cosigüina in the Bay of Fonseca, commonly called the Bay of Conchagua, on the western coast of Central America. *Philosophical Transactions of the Royal Society of London* **126**, 27–30.

Caricchi, L., Annen, C., Blundy, J., Simpson, G. & Pinel, V. (2014). Frequency and magnitude of volcanic eruptions controlled by magma injection and buoyancy. *Nature Geoscience* **7**, 126–130.

Carr, M. J., Saginor, I., Alvarado, G. E., Bolge, L. L., Lindsay, F. N., Milidakis, K., Turrin, B. D., Feigenson, M. D. & Swisher, C. C. (2007). Element fluxes from the volcanic front of Nicaragua and Costa Rica. *Geochemistry, Geophysics, Geosystems* **8**, Q06001.

Cherniak, D. J. (2010). Cation diffusion in feldspars. In: Zhang, Y. & Cherniak, D. J. (eds) *Diffusion in Minerals and Melts. Mineralogical Society of America and Geochemical Society, Reviews in Mineralogy and Geochemistry* **72**, 691–733.

Cioni, R. (2000). Volatile content and degassing processes in the AD 79 magma chamber at Vesuvius (Italy). *Contributions to Mineralogy and Petrology* **140**, 40–54.

Cioni, R., Civetta, L., Marianelli, P., Metrich, N., Santacroce, R. & Sbrana, A. (1995). Compositional layering and syn-eruptive mixing of a periodically refilled shallow magma chamber: the AD 79 Plinian eruption of Vesuvius. *Journal of Petrology* **36**, 739–776.

Cioni, R., Santacroce, R. & Sbrana, A. (1999). Pyroclastic deposits as a guide for reconstructing the multi-stage evolution of the Somma–Vesuvius Caldera. *Bulletin of Volcanology* **61**, 207–222.

Civetta, L., Galati, R. & Santacroce, R. (1991). Magma mixing and convective compositional layering within the Vesuvius magma chamber. *Bulletin of Volcanology* **53**, 287–300.

Clynne, M. A. (1999). A complex magma mixing origin for rocks erupted in 1915, Lassen Peak, California. *Journal of Petrology* **40**, 105–132.

Condomines, M., Tanguy, J.-C. & Michaud, V. (1995). Magma dynamics at Mt Etna: Constraints from U–Th–Ra–Pb radioactive disequilibria and Sr isotopes in historical lavas. *Earth and Planetary Science Letters* **132**, 25–41.

Costa, F. & Morgan, D. (2010). Time constraints from chemical equilibration in magmatic crystals. In: Dosseto, A., Turner, S. P. & Van Orman, J. A. (eds) *Timescales of Magmatic Processes: From Core to Atmosphere*. Chichester: John Wiley, pp. 125–159.

Costa, F. & Singer, B. (2002). Evolution of Holocene dacite and compositionally zoned magma, Volcán San Pedro, Southern Volcanic Zone, Chile. *Journal of Petrology* **43**, 1571–1593.

Costa, F., Chakraborty, S. & Dohmen, R. (2003). Diffusion coupling between trace and major elements and a model for calculation of magma residence times using plagioclase. *Geochimica et Cosmochimica Acta* **67**, 2189–2200.

Costa, F., Scaillet, B. & Pichavant, M. (2004). Petrological and experimental constraints on the pre-eruption conditions of Holocene dacite from Volcán San Pedro (36°S, Chilean Andes) and the importance of sulphur in silicic subduction-related magmas. *Journal of Petrology* **45**, 855–881.

Crank, J. (1975). *The Mathematics of Diffusion*. New York: Oxford University Press.

Darwin, C. (1840). On the connexion of certain volcanic phenomena in South America; and on the formation of mountain chains and volcanos, as the effect of the same power by which continents are elevated. *Transactions of the Geological Society of London, Series 2* **5**, 601–631.

Deering, C., Bachmann, O. & Vogel, T. (2011). The Ammonia Tanks Tuff: Erupting a melt-rich rhyolite cap and its remobilized crystal cumulate. *Earth and Planetary Science Letters* **310**, 518–525.

Devine, J. D., Sigurdsson, H., Davis, A. N. & Self, S. (1984). Estimates of sulfur and chlorine yield to the atmosphere from volcanic eruptions and potential climatic effects. *Journal of Geophysical Research* **89**, 6309–6325.

Devine, J. D., Gardner, J. E., Brack, H. P., Layne, G. D. & Rutherford, M. J. (1995). Comparison of microanalytical methods for estimating H_2O contents of silicic volcanic glasses. *American Mineralogist* **80**, 319–328.

Devine, J. D., Rutherford, M. J., Norton, G. E. & Young, S. R. (2003). Magma storage region processes inferred from geochemistry of Fe–Ti oxides in andesitic magma, Soufrière Hills volcano, Montserrat, W.I. *Journal of Petrology* **44**, 1375–1400.

Druitt, T. & Bacon, C. (1989). Petrology of the zoned calcalkaline magma chamber of Mount Mazama, Crater Lake, Oregon. *Contributions to Mineralogy and Petrology* **101**, 245–259.

Druitt, T. H., Costa, F., Deloule, E., Dungan, M. & Scaillet, B. (2012). Decadal to monthly timescales of magma transfer and reservoir growth at a caldera volcano. *Nature* **482**, 77–80.

Dufek, J. & Bachmann, O. (2010). Quantum magmatism: Magmatic compositional gaps generated by melt–crystal dynamics. *Geology* **38**, 687–690.

France, L., Ildefonse, B., Koepke, J. & Bech, F. (2010). A new method to estimate the oxidation state of basaltic series from microprobe analyses. *Journal of Volcanology and Geothermal Research* **189**, 340–346.

Frost, B. R. & Lindsley, D. H. (1991). Occurrence of iron–titanium oxides in igneous rocks. In: Lindsley, D. H. (ed.) *Oxide Minerals. Mineralogical Society of America, Reviews in Mineralogy* **25**, 433–468.

Galindo, J. (1835*a*). Eruption of the volcano Cosigüina. *American Journal of Science* **28**, 332–336.

Galindo, J. (1835*b*). On the eruption of the volcano Cosigüina, in Nicaragua, 17th January, 1835. *Journal of the Royal Geographical Society of London* **5**, 387–392.

Gao, C., Robock, A. & Ammann, C. (2008). Volcanic forcing of climate over the past 1500 years: An improved ice core-based index for climate models. *Journal of Geophysical Research* **113**, D23111.

Ghiorso, M. S. & Evans, B. W. (2008). Thermodynamics of rhombohedral oxide solid solutions and a revision of the Fe–Ti two-oxide geothermometer and oxygen-barometer. *American Journal of Science* **308**, 957–1039.

Ghiorso, M. S. & Sack, R. O. (1995). Chemical transfer in magmatic processes IV. A revised and internally consistent thermodynamic model for the interpolation and extrapolation of liquid–solid equilibria in magmatic systems at elevated temperatures and pressures. *Contributions to Mineralogy and Petrology* **119**, 197–212.

Giordano, D., Russell, J. K. & Dingwell, D. B. (2008). Viscosity of magmatic liquids: A model. *Earth and Planetary Science Letters* **271**, 123–134.

Harrison, T. M. & Watson, E. B. (1984). The behavior of apatite during crustal anatexis: equilibrium and kinetic considerations. *Geochimica et Cosmochimica Acta* **48**, 1467–1477.

Hawkesworth, C., George, R., Turner, S. & Zellmer, G. (2004). Time scales of magmatic processes. *Earth and Planetary Science Letters* **218**, 1–16.

Hawkesworth, C. J., Blake, S., Evans, P., Hughes, R., Macdonald, R., Thomas, L. E., Turner, S. P. & Zellmer, G. (2000). Time scales of crystal fractionation in magma chambers—Integrating physical, isotopic and geochemical perspectives. *Journal of Petrology* **41**, 991–1006.

Hildreth, W. (1983). The compositionally zoned eruption of 1912 in the Valley of Ten Thousand Smokes, Katmai National Park, Alaska. *Journal of Volcanology and Geothermal Research* **18**, 1–56.

Hildreth, W. & Fierstein, J. (2000). Katmai volcanic cluster and the great eruption of 1912. *Geological Society of America Bulletin* **112**, 1594–1620.

Hildreth, W. & Fierstein, J. (2012). *The Novarupta–Katmai eruption of 1912—largest eruption of the twentieth century: centennial perspectives. US Geological Survey Professional Papers* **1791**.

Hole, M. J., Saunders, A. D., Marriner, G. F. & Tarney, J. (1984). Subduction of pelagic sediments: implications for the origin of Ce-anomalous basalts from the Mariana Islands. *Journal of the Geological Society, London* **141**, 453–472.

Hradecký, P. & Rapprich, V. (2008). Historical tephra-stratigraphy of the Cosigüina volcano (Western Nicaragua). *Revista Geológica de América Central* **38**, 65–79.

Hradecký, P., Havlicek, P., Opletal, M., Rapprich, V., Sebesta, J., Sevcik, J. & Mayorga, E. (2001). *Estudio geológico y reconocimiento de amenazas geológicas en el Volcán Cosiguüina, Nicaragua*, CGU and INETER, Managua, pp. 1–50.

Humphreys, M. C. S., Kearns, S. L. & Blundy, J. D. (2006). SIMS investigation of electron-beam damage to hydrous, rhyolitic glasses: Implications for melt inclusion analysis. *American Mineralogist* **91**, 667–679.

Jarosewich, E., Nelen, J. A. & Norberg, J. A. (1980). Reference samples for electron microprobe analysis. *Geostandards and Geoanalytical Research* **4**, 43–47.

Jochum, K. P., Nohl, U., Herwig, K., Lammel, E., Stoll, B. & Hofmann, A. W. (2005). GeoReM: A new geochemical database for reference materials and isotopic standards. *Geostandards and Geoanalytical Research* **29**, 333–338.

Kelley, K. A. & Cottrell, E. (2009). Water and the oxidation state of subduction zone magmas. *Science* **325**, 605–607.

Kelley, K. A. & Cottrell, E. (2012). The influence of magmatic differentiation on the oxidation state of Fe in a basaltic arc magma. *Earth and Planetary Science Letters* **329–330**, 109–121.

Kilinc, A., Carmichael, I. S. E., Rivers, M. L. & Sack, R. O. (1983). The ferric–ferrous ratio of natural silicate liquids equilibrated in air. *Contributions to Mineralogy and Petrology* **83**, 136–140.

Kutterolf, S., Freundt, A. & Burkert, C. (2011). Eruptive history and magmatic evolution of the 1·9 kyr Plinian dacitic Chiltepe Tephra from Apoyeque volcano in west–central Nicaragua. *Bulletin of Volcanology* **73**, 811–831.

Lamb, H. H. (1970). Volcanic dust in the atmosphere; with a chronology and assessment of its meteorological significance. *Philosophical Transactions of the Royal Society of London* **266**, 425–533.

Landi, P., Bertagnini, A. & Rosi, M. (1999). Chemical zoning and crystallization mechanisms in the magma chamber of the Pomici di Base plinian eruption of Somma–Vesuvius (Italy). *Contributions to Mineralogy and Petrology* **135**, 179–197.

Lange, R. A., Frey, H. M. & Hector, J. (2009). A thermodynamic model for the plagioclase–liquid hygrometer/thermometer. *American Mineralogist* **94**, 494–506.

Lowenstern, J. B. (1993). Evidence for a copper-bearing fluid in magma erupted at the Valley of Ten Thousand Smokes, Alaska. *Contributions to Mineralogy and Petrology* **114**, 409–421.

Malfait, W. J., Seifert, R., Petitgirard, S., Perrillat, J.-P., Mezouar, M., Ota, T., Nakamura, E., Lerch, P. & Sanchez-Valle, C. (2014). Supervolcano eruptions driven by melt buoyancy in large silicic magma chambers. *Nature Geoscience* **7**, 122–125.

Mandeville, C. W., Carey, S. & Sigurdsson, H. (1996). Magma mixing, fractional crystallization and volatile degassing during the 1883 eruption of Krakatau volcano, Indonesia. *Journal of Volcanology and Geothermal Research* **74**, 243–274.

Mandeville, C. W., Webster, J. D., Tappen, C., Taylor, B. E., Timbal, A., Sasaki, A., Hauri, E. & Bacon, C. R. (2009). Stable isotope and petrologic evidence for open-system degassing during the climactic and pre-climactic eruptions of Mt. Mazama, Crater Lake, Oregon. *Geochimica et Cosmochimica Acta* **73**, 2978–3012.

Manga, M. & Brodsky, E. (2006). Seismic triggering of eruptions in the far field: volcanoes and geysers. *Annual Review of Earth and Planetary Sciences* **34**, 263–291.

Marsh, B. D. (1981). On the crystallinity, probability of occurrence, and rheology of lava and magma. *Contributions to Mineralogy and Petrology* **78**, 85–98.

Martel, C., Pichavant, M., Holtz, F., Scaillet, B., Bourdier, J.-L. & Traineau, H. (1999). Effects of fO_2 and H_2O on andesite phase relations between 2 and 4 kbar. *Journal of Geophysical Research* **104**, 29453–29470.

Moore, G., Vennemann, T. & Carmichael, I. S. E. (1998). An empirical model for the solubility of H_2O in magmas to 3 kilobars. *American Mineralogist* **83**, 36–42.

Murphy, M. D., Sparks, R. S. J., Barclay, J., Carroll, M. R., Lejeune, A. M., Brewer, T. S., Macdonald, R., Black, S. & Young, S. (1998). The role of magma mixing in triggering the current eruption at the Soufrière Hills Volcano, Montserrat, West Indies. *Geophysical Research Letters* **25**, 3433–3436.

Nelson, S. T. & Montana, A. (1992). Sieve-textured plagioclase in volcanic rocks produced by rapid decompression. *American Mineralogist* **77**, 1242–1249.

Newhall, C. G. & Self, S. (1982). The Volcanic Explosivity Index (VEI): An estimate of explosive magnitude for historical volcanism. *Journal of Geophysical Research* **87**, 1231–1238.

Palais, J. M. & Sigurdsson, H. (1989). Petrologic evidence of volatile emissions from major historic and pre-historic volcanic eruptions. In: Berger, A., Dickinson, R. E. & Kidson, J. W. (eds). *In: Understanding Climate Change. American Geophysical Union, Geophysical Monograph* **52**, 31–53.

Panjasawatwong, Y., Danyushevsky, L., Crawford, A. & Harris, K. (1995). An experimental study of the effects of melt composition on plagioclase–melt equilibria at 5 and 10 kbar: implications for the origin of magmatic high-An plagioclase. *Contributions to Mineralogy and Petrology* **118**, 420–432.

Papale, P. (1999). Modeling of the solubility of a two-component $H_2O + CO_2$ fluid in silicate liquids. *American Mineralogist* **84**, 477–492.

Petrelli, M., Poli, G., Perugini, D. & Peccerillo, A. (2005). PetroGraph: A new software to visualize, model, and present geochemical data in igneous petrology. *Geochemistry, Geophysics, Geosystems* **6**, Q07011.

Pichavant, M., Martel, C., Bourdier, J.-L. & Scaillet, B. (2002). Physical conditions, structure, and dynamics of a zoned magma

chamber: Mount Pelée (Martinique, Lesser Antilles Arc). *Journal of Geophysical Research* **107**, ECV 1–1–ECV 1-28.

Plank, T. & Langmuir, C. H. (1998). The chemical composition of subducting sediment and its consequences for the crust and mantle. *Chemical Geology* **145**, 325–394.

Putirka, K., Mikaelian, H., Ryerson, F. & Shaw, H. (2003). New clinopyroxene–liquid thermobarometers for mafic, evolved, and volatile-bearing lava compositions, with applications to lavas from Tibet and the Snake River Plain, Idaho. *American Mineralogist* **88**, 1542–1554.

Putirka, K. D. (2005). Igneous thermometers and barometers based on plagioclase + liquid equilibria: Tests of some existing models and new calibrations. *American Mineralogist* **90**, 336.

Putirka, K. D. (2008). Thermometers and barometers for volcanic systems. In: Putirka, K. D. & Tepley, F. J., III (eds) *Minerals, Inclusions and Volcanic Processes. Mineralogical Society of America and Geochemical Society, Reviews in Mineralogy and Geochemistry* **69**, 61–120.

Reclus, E. (1891). *Nouvelle Géographie Universelle*. Paris: Hachette.

Robock, A. (2002). Pinatubo eruption: The climatic aftermath. *Science* **295**, 1242–1244.

Rogers, N. W., Evans, P. J., Blake, S., Scott, S. C. & Hawkesworth, C. J. (2004). Rates and timescales of fractional crystallization from ^{238}U–^{230}Th–^{226}Ra disequilibria in trachyte lavas from Longonot volcano, Kenya. *Journal of Petrology* **45**, 1747–1776.

Roscoe, R. (1952). The viscosity of suspensions of rigid spheres. *British Journal of Applied Physics* **3**, 267–269.

Ruprecht, P., Bergantz, G. W., Cooper, K. M. & Hildreth, W. (2012). The crustal magma storage system of Volcán Quizapu, Chile, and the effects of magma mixing on magma diversity. *Journal of Petrology* **53**, 801–840.

Rutherford, M. J. & Devine, J. D. (1988). The May 18, 1980, eruption of Mount St. Helens 3. Stability and chemistry of amphibole in the magma chamber. *Journal of Geophysical Research* **93**, 11949–11959.

Scaillet, B., Luhr, J. F. & Carroll, M. R. (2003). Petrological and volcanological constraints on volcanic sulfur emissions to the atmosphere. In: Robock, A. & Oppenheimer, C. (eds) *Volcanism and the Earth's Atmosphere. American Geophysical Union, Geophysical Monograph* **139**, 11–40.

Scott, W., Gardner, C., Devoli, G. & Alvarez, A. (2006). The A.D. 1835 eruption of Volcán Cosigüina, Nicaragua: A guide for assessing local volcanic hazards. In: Rose, W. I., Bluth, G. J. S., Carr, M. J., Ewert, J. W., Patino, L. C. & Vallance, J. W. (eds) *Volcanic Hazards in Central America. Geological Society of America, Special Papers* **412**, 167–187.

Self, S., Rampino, M. & Carr, M. (1989). A reappraisal of the 1835 eruption of Cosigüina and its atmospheric impact. *Bulletin of Volcanology* **52**, 57–65.

Siebert, L. & Simkin, T. (2002). *Volcanoes of the World: an Illustrated Catalog of Holocene Volcanoes and their Eruptions. Smithsonian Institution, Global Volcanism Program Digital Information Series*, **GVP-3** (http://www.volcano.si.edu/world/).

Sisson, T. W. & Bacon, C. R. (1999). Gas-driven filter pressing in magmas. *Geology* **27**, 613–616.

Sparks, R. S. J. (2003). Forecasting volcanic eruptions. *Earth and Planetary Science Letters* **210**, 1–15.

Sparks, S. R. J., Sigurdsson, H. & Wilson, L. (1977). Magma mixing: a mechanism for triggering acid explosive eruptions. *Nature* **267**, 315–318.

Spera, F. J. (2000). Physical properties of magma. In: Sigurdsson, H., Houghton, B., McNutt, S. R., Rymer, H. & Stix, J. (eds) *Encyclopedia of Volcanoes*. San Diego, CA: Academic Press, pp. 171–190.

Stix, J. & Kobayashi, T. (2008). Magma dynamics and collapse mechanisms during four historic caldera-forming events. *Journal of Geophysical Research* **113**, B09205.

Stix, J., Gauthier, G. & Ludden, J. N. (1995). A critical look at quantitative laser-ablation ICP-MS analysis of natural and synthetic glasses. *Canadian Mineralogist* **33**, 435–444.

Stormer, J. C. & Nicholls, J. (1978). XLFRAC: a program for the interactive testing of magmatic differentiation models. *Computers and Geosciences* **4**, 143–159.

Stormer, J. C., Pierson, M. L. & Tacker, R. C. (1993). Variation of F and Cl X-ray intensity due to anisotropic diffusion in apatite during electron microprobe analysis. *American Mineralogist* **78**, 641–648.

Tait, S., Jaupart, C. & Vergniolle, S. (1989). Pressure, gas content and eruption periodicity of a shallow, crystallising magma chamber. *Earth and Planetary Science Letters* **92**, 107–123.

Van Orman, J. A., Cherniak, D. J. & Kita, N. T. (2014). Magnesium diffusion in plagioclase: Dependence on composition, and implications for thermal resetting of the ^{26}Al–^{26}Mg early solar system chronometer. *Earth and Planetary Science Letters* **385**, 79–88.

Widom, E., Schmincke, H. U. & Gill, J. B. (1992). Processes and timescales in the evolution of a chemically zoned trachyte: Fogo A, São Miguel, Azores. *Contributions to Mineralogy and Petrology* **111**, 311–328.

Williams, H. (1952). The great eruption of Coseguina, Nicaragua, in 1835, with notes on the Nicaraguan volcanic chain. *University of California Publications in Geological Sciences* **29**, 21–46.

Zellmer, G. F., Blake, S., Vance, D., Hawkesworth, C. & Turner, S. (1999). Plagioclase residence times at two island arc volcanoes (Kameni Islands, Santorini, and Soufrière, St. Vincent) determined by Sr diffusion systematics. *Contributions to Mineralogy and Petrology* **136**, 345–357.